

UNIVERSITY OF TWENTE.

Faculty of Engineering Technology

MODELING OF MAGNETOCALORIC REFRIGERATION WITH PACKED BED REGENERATOR

Abdan Hanif Satria Budiman

M.Sc. Thesis

November 2016

Chairman:

Prof. Dr. Ir. T.H. van der Meer

Exam committee:

Prof. Dr. Ir. T.H. van der Meer

Dr. Ir. G.G.M. Stoffels

Dr. Ir. S. Vanapalli

Thermal Engineering Group

Faculty of Engineering Technology

University of Twente

P.O. Box 217

7500 AE Enschede

The Netherlands

Preface

Firstly, I would like to express my sincere gratitude to Professor Theo van der Meer for the guidance, support, discussion, and inspiration during the completion of this thesis assignment. His help also gave me an excellent opportunity to take a Double Degree program between the ITB Indonesia and the University of Twente.

Completion of this thesis was also greatly helped by the involvement of colleagues in the Thermal Engineering Group whose doing research in the field of magnetocaloric. The weekly discussion with was very positive for the progress of this thesis.

My participation in this master program can also occur on a scholarship provided by the company where I worked, PT PLN (Persero). I feel very fortunate and thankful for the opportunity that has given to me.

I am also grateful to all Indonesian friend that give me a "home atmosphere" during my time in Enschede.

Las but not least, I would like to express my deep gratitude to my wife and my daughter for the support and endless love. As well as both of my parents for their prayer.

Abdan Hanif Satria Budiman
Enchede, November 2016

Summary

Cooling by vapor compression is currently the most widely used technology for refrigeration or heat pump systems. Vapor compression itself is a 100-year-old technology that uses refrigerants which potentially cause problems to the environment especially related to ozone depletion and global warming. The system also requires a compressor that is a weakness as it dissipates noise and vibrations.

One of the alternative technologies to vapor compression cooling is magnetic refrigeration that works based on the magnetocaloric effect (MCE) which no longer utilizes the refrigerants. Currently, the magnetocaloric refrigeration system with an active magnetic regenerator (AMR) is considered as the best one to create sufficient temperature span between the cold and hot region for a practical cooling device. However, the active magnetic regenerative refrigerator (AMRR) cannot break the vapor compression cooling dominance yet since it has an inferior overall performance.

The performance can be upgraded with a better heat transfer between the MCM and the working fluid. Compared to a straight channel configuration, a spherical packed-bed regenerator has better heat transfer characteristics since it has a larger heat transfer area over the same volume.

At room temperature, the system should utilize a suitable MCM. Gadolinium (Gd) is one of the MCMs with the Curie point near room temperature (around 293 K). Since Gd is a rare-earth material, it is necessary to search for a replacement for the material. The cheap and non-toxic MnFe(P,Si) compound is a promising candidate for Gd alternative.

This study investigates and compares the performance of an AMRR with spherical packed-bed regenerator made from Gd and four layers of MnFe(P,Si) compound with different (P,Si) compositions, by numerical simulations using commercial software COMSOL Multiphysics. The compound itself is developed by the Fundamental Aspects of Materials and Energy group of the TU Delft, as reported by their publications. Some interpolations and assumptions of the required magnetocaloric properties are taken to complete the input data.

The model geometry is based on a Gd AMRR experimental device of the University of Ljubljana, Slovenia. The experimental result used to verify the simulation outcome. The study predicts that the AMRR with layered compound has a nearly equal performance to the one with Gd in temperature span wise. On the other hand, the predicted maximum cooling capacity of the system with layered AMR is higher than the system with Gd AMR.

Contents

| | |
|--|------------|
| Preface | iii |
| Summary | v |
| Nomenclature | ix |
| 1 Introduction | 1 |
| 1.1 Background | 1 |
| 1.2 The magnetocaloric effect and magnetocaloric heat pump | 2 |
| 1.3 Objectives and methodology | 4 |
| 1.4 Report organization | 6 |
| 2 Literature study | 7 |
| 2.1 Thermodynamics of the magnetocaloric effects | 7 |
| 2.2 Heat transfer in porous media | 9 |
| 2.3 The active magnetic regenerator (AMR) | 11 |
| 3 Modeling and simulation | 17 |
| 3.1 Active Magnetic Regenerator (AMR) geometry and operational parameter | 17 |
| 3.2 Numerical setup | 20 |
| 3.2.1 The governing equations | 20 |
| 3.2.2 The boundary conditions | 20 |
| 3.2.3 Mesh characteristics | 20 |
| 3.3 Improving the operational setup configuration | 21 |
| 3.4 Inclusion of Magnetocaloric Effects (MCE) | 22 |
| 3.4.1 Gadolinium | 22 |
| 3.4.2 The MnFe(P,X) compound | 24 |
| 3.5 The layered AMR | 25 |
| 4 Result and discussion | 29 |
| 4.1 Validation of the model | 29 |
| 4.1.1 The MCE in Gadolinium AMR model | 29 |
| 4.1.2 Zero cooling load simulation | 32 |
| 4.1.3 Comparison of the temperature span | 35 |

| | | |
|----------|---|-----------|
| 4.2 | The optimized experimental model | 36 |
| 4.2.1 | Zero cooling load simulation | 36 |
| 4.2.2 | Cooling capacity | 37 |
| 4.3 | Optimized model with layered MnFe(P,Si) compound as MCM | 39 |
| 4.3.1 | The MCE in the layered AMR | 39 |
| 4.3.2 | Zero cooling load simulation | 41 |
| 4.3.3 | Cooling capacity | 42 |
| 5 | Conclusions and recommendations | 45 |
| 5.1 | Conclusions | 45 |
| 5.2 | Recommendations | 46 |
| | References | 47 |
| | Appendices | |
| A | Appendix | 51 |
| A.1 | General heat transfer correlation | 51 |
| A.2 | Cooling capacity at f 0.3 Hz | 53 |
| A.3 | COP prediction | 53 |
| A.4 | Pumping work | 55 |
| A.5 | Parasitic heat loss | 56 |
| A.6 | Magnetocaloric properties of the material in the model | 56 |
| A.6.1 | Gadolinium | 57 |
| A.6.2 | The compound | 57 |

Nomenclature

Acronym

| | |
|-------------|--|
| AMR | Active Magnetic Regenerator |
| AMRR | Active Magnetic Regenerative Refrigeration |
| CHEX | Cold Heat Exchanger |
| COP | Coefficient of Performance |
| FOMT | First Order Magnetic Transition |
| SOMT | Second Order Magnetic Transition |
| Gd | Gadolinium |
| HHEX | Hot Heat Exchanger |
| MCE | Magnetocaloric Effects |
| MCM | Magnetocaloric Material |
| VCS | Vapor Compression System |

Roman symbol

| | |
|-----------------------------|--|
| <i>a</i> | Contact surface per unit volume [m^{-1}] |
| <i>c</i> | Specific heat capacity [$J/(kgK)$] |
| <i>f</i> | Operating frequency [Hz] |
| <i>Fo</i> | Fourier number |
| <i>h</i> | Heat transfer coefficient [$W/(m^2K)$] |
| <i>h</i> | Specific enthalpy [J/kg] |
| <i>H</i> | Magnetic field intensity [A/m] |
| <i>\dot{m}</i> | Mass flow rate [kg/s] |
| <i>M</i> | Magnetization [A/m] |
| <i>Nu</i> | Nusselt number |
| <i>p</i> | Pressure [Pa] |
| <i>Pr</i> | Prandtl number |
| <i>\dot{Q}</i> | Volumetric heat flux [W/m^3] |
| <i>Re</i> | Reynolds number |

| | |
|-----|-----------------------|
| s | Entropy [$J/(kgK)$] |
| T | Temperature [K] |
| t | Time [s] |
| u | Velocity [m/s] |
| V | Volume [m^3] |
| W | Work [W] |

Greek symbol

| | |
|---------------|--|
| α | Thermal diffusivity [m^2/s] |
| κ | Permeability [m^2] |
| ε | Porosity |
| μ | Dynamic viscosity [$Pa.s$] |
| μ_0 | Magnetic permeability in vacuum [H/m or N/A^2] |
| ρ | Density [kg/m^3] |
| τ | Dwelling time [s] |

Subscript and superscript

| | |
|-------|---------------|
| c | cold |
| f | fluid |
| h | hot |
| mag | magnetization |
| s | solid |

Introduction

1.1 Background

In 2015, almost 50% energy consumption in Europe was taken by heating and cooling activities [1]. Vapor compression system (VCS) still is the most dominant system used in a refrigeration processes while natural gas combustion holds the dominance for space heating purposes. Vapor compression itself is a 100-year-old technology that uses refrigerants which potentially cause problems to the environment especially related to ozone depletion and global warming. The system also requires a compressor that is a weakness as it dissipates noise and vibrations.

Cooling demands rise rapidly. By 2060 energy consumption worldwide in cooling will overtake that used in heating [2] [3] (see Fig. 1.1). The world not only needs to generate more electricity and heat from renewable sources, but also has to find alternative technologies to make cooling and heating more efficient, and harmless for the environment.

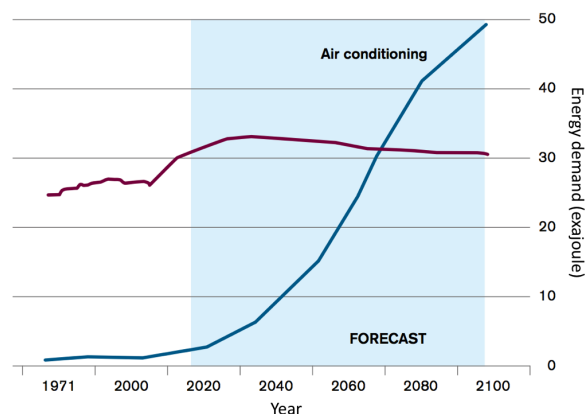


Figure 1.1: Worldwide forecast energy demand (in exajoules) for heating (red line) and cooling (blue line) (picture taken from [4])

One of the alternatives is magnetic refrigeration. The system is based on a phenomena called the magnetocaloric effect that eliminates the vapor refrigerant from the system. As the compressor is also out, one can expect a silent refrigeration system. The system is also commonly addressed as a solid state refrigeration. Electricity is needed to supply the power

for a pump and provide magnetic fields, while a permanent magnet might also provide the latter. The electricity is expected to be generated by renewable energy sources to create a sustainable loop of a larger system.

The magnetic refrigeration in room temperature is becoming an attractive topic for researchers. Porous media material is promising to be used in magnetic refrigeration on the basis that the configuration has an excellent heat transfer characteristic, although with an increase of pressure drop as a drawback. Other research is also emphasizing the discovery of new material that applicable in room temperature refrigeration other than the rare earth material like Gadolinium.

1.2 The magnetocaloric effect and magnetocaloric heat pump

As aforementioned, the magnetic refrigeration is one of the promising alternatives for Vapor Compression System (VCS) technology. It was not the only option since there are others that also has a potential to be widely applied in the near future. The thesis work [5] gives a summary of the alternatives to VCS, the advantages, and weaknesses. Magnetocaloric cooling is considered as a very promising alternative technology [6].

A magnetocaloric heat pump works by the favor of the MCE. The MCE first discovered by the French and Swiss physicist, Weiss and Piccard in 1917 [7]. It has been used in cryogenic cooling since 1930. The simplest expression to explain the MCE is that a particular material, known as the Magnetocaloric Material (MCM), will experience a temperature increase as is exposed to a magnetic field and further the temperature will also decrease if the magnetic field is removed. The applied magnetic field promotes a phase change from ferromagnetic to a paramagnetic state to the material. The magnitude of the increase and decrease of temperature depends on the magnetocaloric properties of the MCM and the strength of the magnetic field source.

In a MCM, the total entropy is related to the magnetic part (i.e. the magnetic entropy), and other contribution related to the temperature of the system (i.e. the lattice entropy). The magnetic moment in the MCM is not at uniform orientation when it is outside the magnetic field, but it will immediately turn to the similar direction once is inside (see Fig. 1.2). The level of order is then increasing, which implies the decrease in the magnetic entropy. In an isentropic (adiabatic) system, when the total entropy is not changing, the lattice entropy has to increase. Hence the temperature is elevated. Further explanation is given in Chapter 2 Section 2.1 that explain the thermodynamics of magnetocaloric effect.

Magnetocaloric characteristics of MCM can be divided into two categories based on the order of their phase transition, namely the second order and the first order materials (see Fig. 1.3). The change occurs at a certain temperature, called the Curie temperature (T_{curie}), at which the MCE occurred the strongest. This situation is mathematically explained in Chapter 2.

The transition in the first order material takes place in a narrow temperature range, which also means a sudden change in magnetization, as shown in Fig. 1.3 (b). The abrupt change

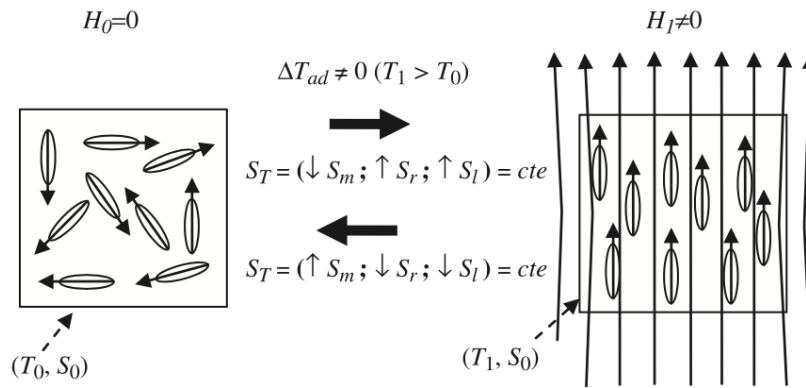


Figure 1.2: Arrangement of the magnetic moment spin system of an adiabatic system off and on and in a magnetic field (picture source: [8])

in magnetization creates a strong magnetocaloric effect because the strength of the MCE is parallel to the change of magnetization with respect to temperature. The derivation of the equation is presented in Chapter 2. The MCE in a first order material is often called a giant magnetocaloric effect.

Despite having a strong effect, a single type of first order material is not suitable for Active Magnetic Regenerative Refrigeration (AMRR) application because the MCE is only available in a short temperature range. The MnFe(P,Si) compound is an example of a first order MCM.

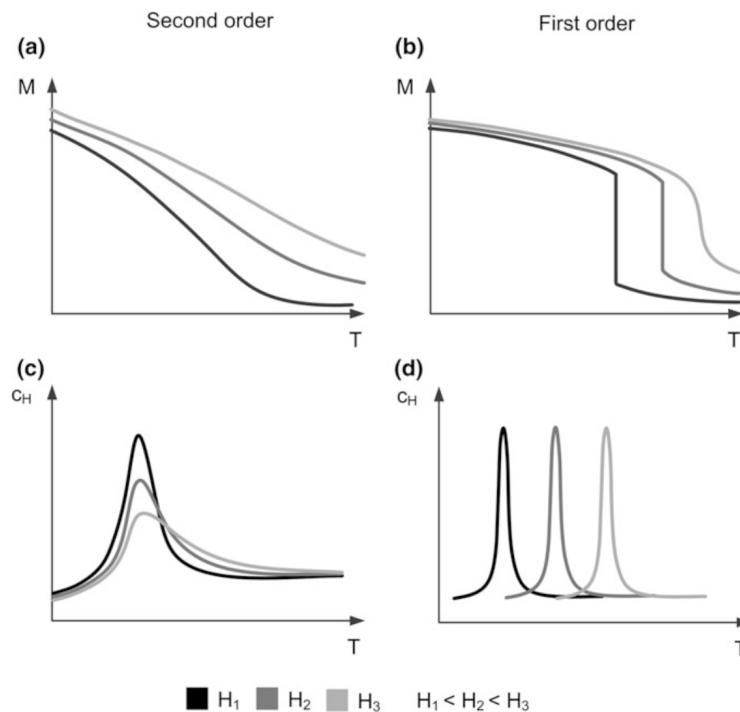


Figure 1.3: The second order and the first order magnetocaloric material characteristics (picture taken from [9])

Contrary to the first order, the second order material cover a wider working temperature

range of the MCE as indicated by the transition of internal magnetization. This type of MCM is valuable in the AMRR application as it can hold significant MCE although the temperature is deviating from the Curie point. Gadolinium is an example of a second order material that has Curie point around room temperature.

The working principle of a magnetocaloric heat pump can be understood by comparing it to the VCS. Fig. 1.4 shows the schematic of a magnetocaloric heat pump cycle analogical with vapor compression, which generally consists of four steps as the following:

- A VCS requires mechanical energy input to compress the vapor refrigerant, while a magnetocaloric refrigeration requires input of energy to magnetize the MCM (that acts as a solid refrigerant).
- As the vapor refrigerant is compressed, analogically the solid refrigerant is magnetized (which makes their temperature increased and higher than the environment); the refrigerant then rejects heat to the environment.
- Expansion process cools down the vapor refrigerant even further, accordingly the demagnetization decreases the MCM temperature.
- The refrigerant is then able to absorb heat from the area that is to be cooled.

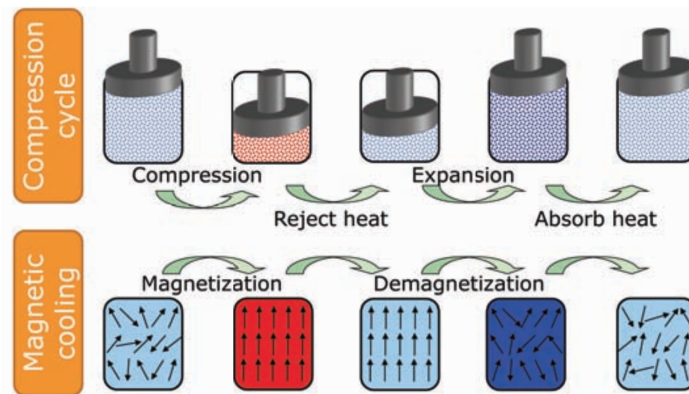


Figure 1.4: Analogical work steps of magnetocaloric heat pump to vapor compression system (picture taken from [10])

The analogy to gas compression can also be made to understand the related work, as illustrated by Fig. 1.5. Both schemes show a closed system. In gas compression, work is done by the piston to compress the gas in the cylinder, while in a magnetocaloric system work is done by the magnetic field.

1.3 Objectives and methodology

The primary objective of the study is to analyze the transport of energy in a magnetocaloric heat pump with spherical packed bed AMR by building a representative model. The study

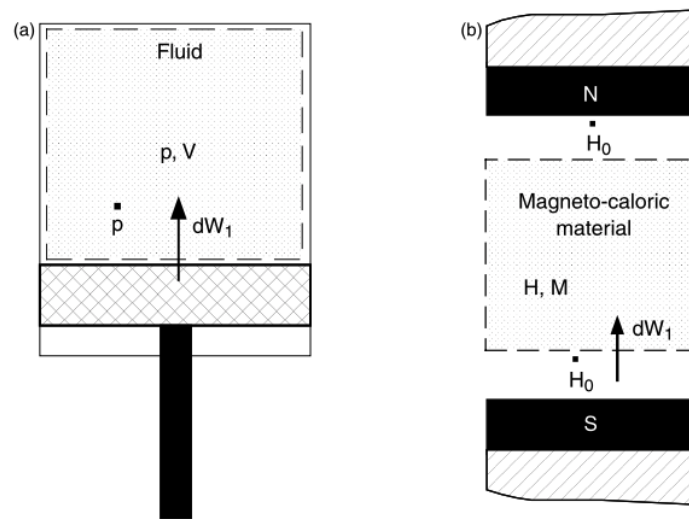


Figure 1.5: Analogy of adiabatic process in a gas compression system (a) with a magneto-caloric process (b) (picture taken from [11])

also aims to see if the available MCM, as an alternative for rare-earth material Gadolinium, is feasible for room temperature application.

The energy transport phenomena are related to the heat transfer between the working fluid and the porous media made from a MCM. The fluid flows through spaces between packed spherical particles of the MCM. The model is expected to be able to predict the performances of the related system. The following methods are taken to reach the objectives as mentioned above:

- Build a model using commercial software, COMSOL Multiphysics, that numerically solves the transport of energy in the system.
- Verify the model by comparing the result of numerical solution given by the model with the available references. The chosen references is a results from an experimental study reported by [12] which utilize Gadolinium (Gd) as MCM.
- Use the model to investigate the performance of a AMRR system with synthesized MCM made from MnFe(P, Si) compound.

To be focused on to the objectives; the following research questions are determined:

1. *Is it representative to model a magnetocaloric heat pump with spherical packed bed AMR with one-dimensional model in COMSOL Multiphysics?*
2. *How does the performance of the packed bed AMRR system with MnFe(P, Si) compound as MCM compare to the one with Gd?*

1.4 Report organization

This report consist of five main chapters starting with an introductory chapter explaining the background on why the alternative technologies for refrigeration and space heating are developed. This chapter also includes the objective and the methodology of the study.

Chapter 2 gives the basic knowledge including the related theories of the magnetocaloric effects; the working principle of an AMRR about its thermodynamic cycle; it also explains the energy transport in porous media between the fluid and the solid.

Chapter 3 delivers the information on how the model is built as the governing equations, the boundary conditions, the assumptions and other physical condition described. This chapter also includes the explanation of the method of integrating the magnetocaloric effects phenomena into the model.

Chapter 4 shows the results of the numerical simulations and the detailed analysis and discussion. Finally, the conclusion and recommendation of the study are presented by Chapter 5.

Literature study

2.1 Thermodynamics of the magnetocaloric effects

To comprehend the thermodynamics of the magnetocaloric effects, some mathematical terms are derived. The derivation is necessary to understand how the MCE is mathematically quantified and integrated into the model as the heat source term or as the adiabatic temperature increase. The first law of thermodynamics for a closed system can be expressed as:

$$du = \delta q - \delta w \quad (2.1)$$

which implies the internal energy will increase if heat is added or work performed on the MCM. In this case, the work is done to the MCM as it moved into the magnetic field which also causes the internal magnetization of the MCM to increase. This work is mathematically expressed as:

$$dw = -\mu_0 H dM \quad (2.2)$$

substituting the above two equations, gives:

$$du = dq + \mu_0 H dM \quad (2.3)$$

apply the second law of thermodynamics for a reversible process:

$$dq = T ds \quad (2.4)$$

makes the internal energy expressed as:

$$du = T ds + \mu_0 H dM \quad (2.5)$$

The components of total entropy in a system consist of lattice entropy (S_L), electric entropy (S_E), and magnetic entropy (S_M). In an adiabatic system, the S_M is the one that changes if the domain is exposed to a changing magnetic field. Therefore, the (specific) entropy is not only a function of temperature but also a function of magnetic field strength.

Since the entropy is dependent on T and H, if a derivative of the total entropy is taken,

then it will give:

$$ds(T, H) = \left(\frac{\partial s}{\partial T} \right)_H dT + \left(\frac{\partial s}{\partial H} \right)_T dH \quad (2.6)$$

Considering Eq. 2.4, in an adiabatic condition, one can rewrite Eq. 2.6 to:

$$\left(\frac{\partial s}{\partial T} \right)_H dT = - \left(\frac{\partial s}{\partial H} \right)_T dH \quad (2.7)$$

Substituting Eq. 2.6 to 2.4 gives the expression of the specific heat and the specific heat capacity:

$$dq = c_H(T, H)dT + c_T(T, H)dH \quad (2.8)$$

thus,

$$c_H = \left(\frac{\partial q}{\partial T} \right)_H = T \left(\frac{\partial s}{\partial T} \right)_H \quad (2.9)$$

$$c_T = \left(\frac{\partial q}{\partial H} \right)_T = T \left(\frac{\partial s}{\partial H} \right)_T \quad (2.10)$$

Rewriting Eq. 2.7 considering 2.9, gives:

$$dT = - \left(\frac{T}{c_H} \right) \left(\frac{\partial s}{\partial H} \right)_T dH \quad (2.11)$$

with Maxwell relation,

$$\left(\frac{\partial s}{\partial H} \right)_T = \mu_0 \left(\frac{\partial M}{\partial T} \right)_H \quad (2.12)$$

The Eq. 2.11, which defines the adiabatic temperature change, can also be written as:

$$dT = - \left(\frac{T}{c_H} \right) \mu_0 \left(\frac{\partial M}{\partial T} \right)_H dH \quad (2.13)$$

Eq. 2.13 can be expressed in terms of volumetric heat source by moving the c_H to the left hand side and multiply with the density of the material, ρ . This leads to:

$$\rho c_H \frac{dT}{dt} = -\rho \mu_0 T \left(\frac{\partial M}{\partial T} \right)_H \frac{dH}{dt} = \dot{Q}_{MCE} \quad (2.14)$$

This is the source term which can be built in the energy equation. The governing equation, together with the data of internal magnetization and specific heat capacity (as function of magnetic field strength and temperature), are further explained in Chapter 3

The expression of (specific) enthalpy can be defined as:

$$h = u - \mu_0 H M \quad (2.15)$$

The derivative of the specific enthalpy is taken by applying the Eq. 2.5:

$$dh(s, H) = \left(\frac{\partial h}{\partial s} \right)_H ds + \left(\frac{\partial h}{\partial H} \right)_s dH = T ds - \mu_0 M dH \quad (2.16)$$

The isothermal entropy change is presented as a function of the T and H which leads to the following expression:

$$ds(T, H) = \left(\frac{\partial s}{\partial H} \right)_T dH = \mu_0 \left(\frac{\partial M}{\partial T} \right)_H dH \quad (2.17)$$

further, a definite integral to the Eq. 2.17 within two different magnetic fields can be taken to find the isothermal entropy change, Δs .

$$\Delta s = s_2 - s_1 = \int_{H_1}^{H_2} \left(\frac{\partial s}{\partial H} \right)_T dH = \int_{H_1}^{H_2} \mu_0 \left(\frac{\partial M}{\partial T} \right)_H dH = \int_{H_1}^{H_2} \frac{c_T}{T} dH \quad (2.18)$$

Other than isothermal entropy change and adiabatic temperature change, the process of heat transfer during a constant magnetic field (isofield cooling or heating) is also defined. In constant magnetic field, one can take derivative to heat and enthalpy (Eq. 2.4 and 2.16):

$$dq = dh = c_H dT = T \left(\frac{\partial s}{\partial T} \right)_H dT \quad (2.19)$$

2.2 Heat transfer in porous media

Flow velocity in porous media

Porosity (ε) is an important variable in a porous medium. It indicates the proportion of void part of the domain, which makes the part occupied by the solid to be equal to $(1 - \varepsilon)$. Assuming the domain in the model as an isotropic medium, the surface porosity (ratio of void surface to the total cross-sectional area) is equal to ε . This assumption also implies that all pores in the medium connected to each other, from the inlet to the outlet. For beds of solid spheres with a uniform diameter, ε can vary between the limits 0.2595 (rhombohedral packing) and 0.4764 (cubic packing) [13].

Darcy was the first to made a study of an incompressible laminar flow through a solid matrix with nearly uniform-sized particles in 1856 [14]. The schematic result of the research is given in Fig. 2.1 which shows the change of velocity profile from a parabolic at the inlet to a uniform profile after entering the porous media domain. Based on this condition, it is relevant to study the phenomena of the energy transport in porous media by a one-dimensional model. Mathematically, Darcy's findings are formulated Eqs. 2.20.

$$u_D = -\frac{\kappa}{\mu} \frac{\partial p}{\partial x} \quad (2.20)$$

where μ is the viscosity, κ is permeability, and u_D is the darcy flow velocity that describes the averaged velocity inside the pores. In the case of beds of particles or fibers, the permeability is characterized by the porosity and the effective average particle diameter d_p . The hydraulic radius theory of Carman-Kozeny, for a laminar flow, leads to Eq. 2.21. [13].

$$\kappa = \frac{d_p^2 \varepsilon^3}{180(1 - \varepsilon)^2} \quad (2.21)$$

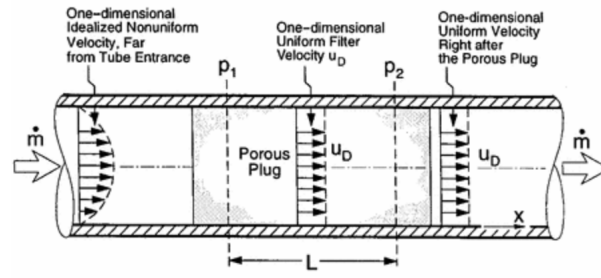


Figure 2.1: Illustration of the velocity profile in porous media (picture taken from [14])

Taking an average of the fluid velocity over a void volume V_f give the intrinsic average velocity u_f , which is related to u_D by the Dupuit-Forchheimer relationship $u_f = \varepsilon u_D$ [13]. In this study, the used working fluid is water (and water-ethylene glycol solution), in which one can assume an incompressible flow.

Using Eq. 2.20 and 2.21, the pressure drop can be determined. Another empirical equation that is widely used in calculating the pressure drop in porous media with uniform spherical particles is suggested by Ergun (Eq. 2.22), which applied in this study.

$$\Delta p = \frac{1}{2} \frac{L \rho_f}{d_h} \left(\frac{133}{Re} + 2.33 \right) \left(\frac{u_D}{\varepsilon} \right)^2 \quad (2.22)$$

The pressure drop along the porous medium is needed to calculate the pumping power (\dot{W}_{pump}) required to flow the working fluid, generally by using the Eq. 2.23. The pump efficiency (η_{pump}) assumed to be 0.8.

$$\dot{W}_{pump} = \frac{\dot{m}_f \Delta p}{\rho_f \eta_{pump}} \quad (2.23)$$

Heat transfer in porous media

In the porous AMR, due to cyclic (de)magnetization and fluid flow, the temperature of the solid MCM (T_s) is different to the temperature of the working fluid (T_f). In other words, there is no thermal equilibrium between the solid and the fluid.

Heat transfer in porous media is governed by two equations, one for the solid and another one for the fluid part, with the consideration of porosity of the porous media. An additional source term is added to couple both governing equations, expressing the exchanged heat between both components.

$$(1 - \varepsilon) \rho_s c_{p,s} \frac{\partial T}{\partial t} = (1 - \varepsilon) k_s \frac{\partial^2 T}{\partial x^2} + h(a_{sf})(T_f - T_s) + \dot{Q}_{MCE} \quad (2.24)$$

$$\varepsilon \rho_f c_{p,f} \frac{\partial T}{\partial t} + \varepsilon \rho_f c_{p,f} u_D \frac{\partial T}{\partial x} = \varepsilon k_f \frac{\partial^2 T}{\partial x^2} + h(a_{sf})(T_s - T_f) \quad (2.25)$$

where the specific surface area (surface per unit volume) a_{sf} is given by:

$$a_{sf} = \frac{6(1 - \varepsilon)}{d_p} \quad (2.26)$$

The heat transfer coefficient for a porous bed is given by Dixon and Cresswell (1979) [13] with particle diameter d_p , the h expressed as:

$$\frac{1}{h} = \frac{d_p}{k_f Nu} + \frac{d_p}{\beta k_s} \quad (2.27)$$

where β is the coefficient of volumetric thermal dispersion which for particle in spherical form, β is equal to 10. The fluid-solid Nusselt number, Nu_{fs} is taken from the study of Wakao and Kaguei [15] that proposed the correlation for a wide range of Reynolds numbers, (Re_p), up to 8500, with the expression shown by Eq. 2.28. The Reynolds number for the fluid flow in the pores of the AMR in this study is less than 100.

$$Nu = 2.0 + 1.1Pr^{1/3}Re_p^{0.6} \quad (2.28)$$

Reynolds number and Prandtl number are defined by:

$$Re = \frac{d_p \rho_f u_D}{\mu} \quad (2.29)$$

$$Pr = \frac{\mu c_{p,f}}{k_f} \quad (2.30)$$

2.3 The active magnetic regenerator (AMR)

Permanent magnets are preferable to be applied as the magnetic field source due to cost constraints. With average magnetic field strength up to 1.5 Tesla, the adiabatic temperature change (ΔT_{ad}) is not more than 5 K. A certain method is needed to create a wider temperature span to become applicable.

The AMR can develop the temperature span to a level that makes the system practical for cooling or heating devices, although the ΔT_{ad} of the MCM is not quite large. The "regenerator" stores and transfers the heat periodically to the working (heat transfer) fluid. Therefore in AMR, the overall performance is not only determined by the magnetocaloric properties of MCM, but also its thermal properties, the manufacturability, and other determinants that influence the heat transfer characteristics.

The process itself follows a thermodynamics cycle, and it can be modeled by a Brayton-like AMR cycle, which its schematic T-s diagram shown in Fig. 2.2. The figure shows the isofield heating/cooling (during hot and cold blow), and the adiabatic-isentropic temperature change (during (de)magnetization).

The process can also be modeled by an Ericsson and a hybrid cycle, as has been done by [16], which gives more flexibility to frequency variation. Fig. 2.3 provides an idea about

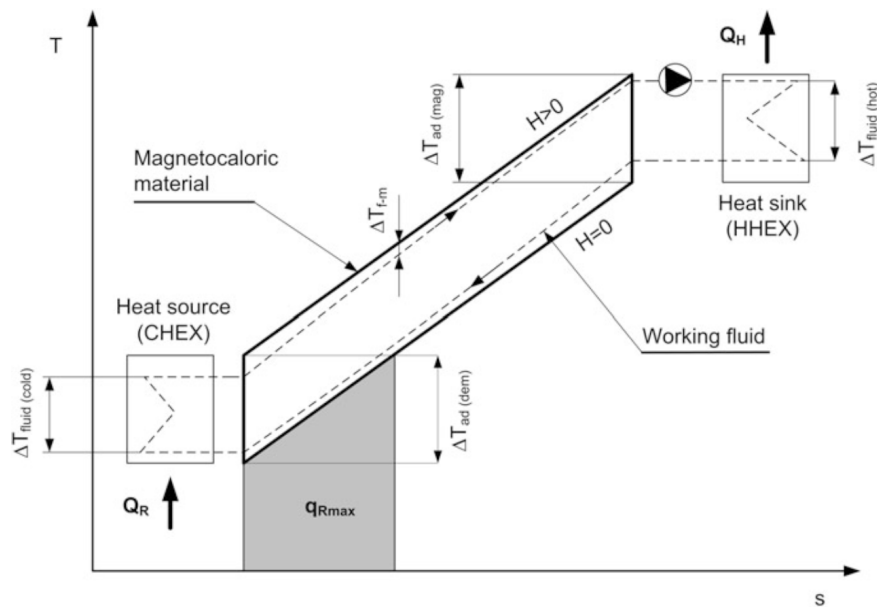


Figure 2.2: Schematic T-s diagram of a Brayton-like AMR cycle (picture taken from [9])

the difference in the behavior of applied magnetic field change and fluid flow profile between the three cycles.

Different with Brayton-like, the fluid flow in the Ericsson-like cycle does not occur during the constant magnetic field. The fluid flow (hot blow) starts together with the magnetization and ends right before the demagnetization. The cold blow immediately begins after the end of the hot blow and finishes some moment after demagnetization is complete. By applying this sequence, the frequency is independent to τ_{mag} and determined only by fluid flow period.

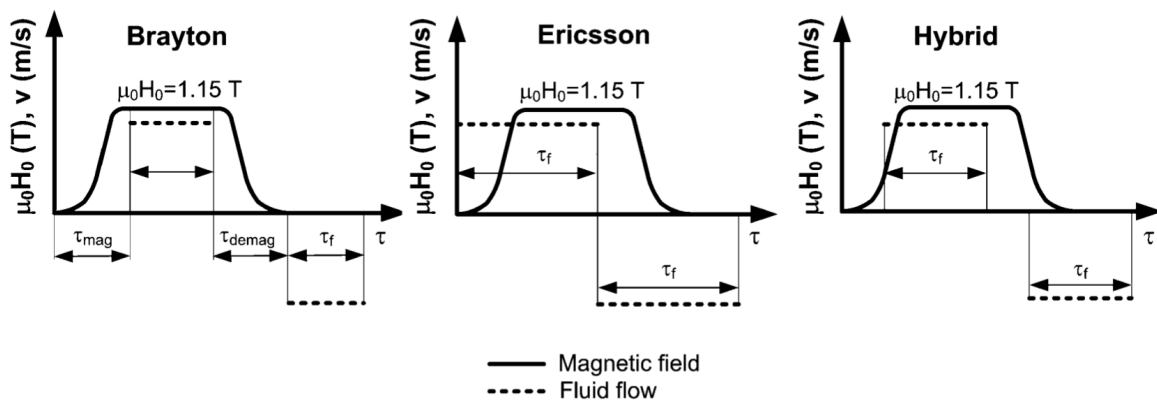


Figure 2.3: The profiles of the applied magnetic field and the fluid flow for three different thermodynamic cycles (picture taken from [9])

An AMRR system consists of a magnetic working body (porous media made from spherical MCM); magnetization system to generate the magnetic field strength; the hot and cold heat exchangers; and heat transfer fluid. Those components work together in such a way

to make a complete thermodynamic cycle. The model built in this study is based on the Brayton-like cycle with the following steps, which illustrated by Fig. 2.4.

- Magnetization: the magnetocaloric material enters the high magnetic field zone, and its temperature is increasing due to magnetocaloric effect (Fig. 2.4 a).
- "The hot blow": the working fluid flows from the cold zone through the magnetized AMR to the hot zone; as it absorbs heat from the AMR and rejects it to the environment (Fig. 2.4 b).
- Demagnetization: the magnetic field is removed from the AMR which immediately decreases its temperature (Fig. 2.4 c).
- "The cold blow": the working fluid flows from the hot zone to the cold zone through the cooled AMR, as it releases the heat to the AMR and become cold enough to absorb heat from the area that is going to be cooled (Fig. 2.4 d).

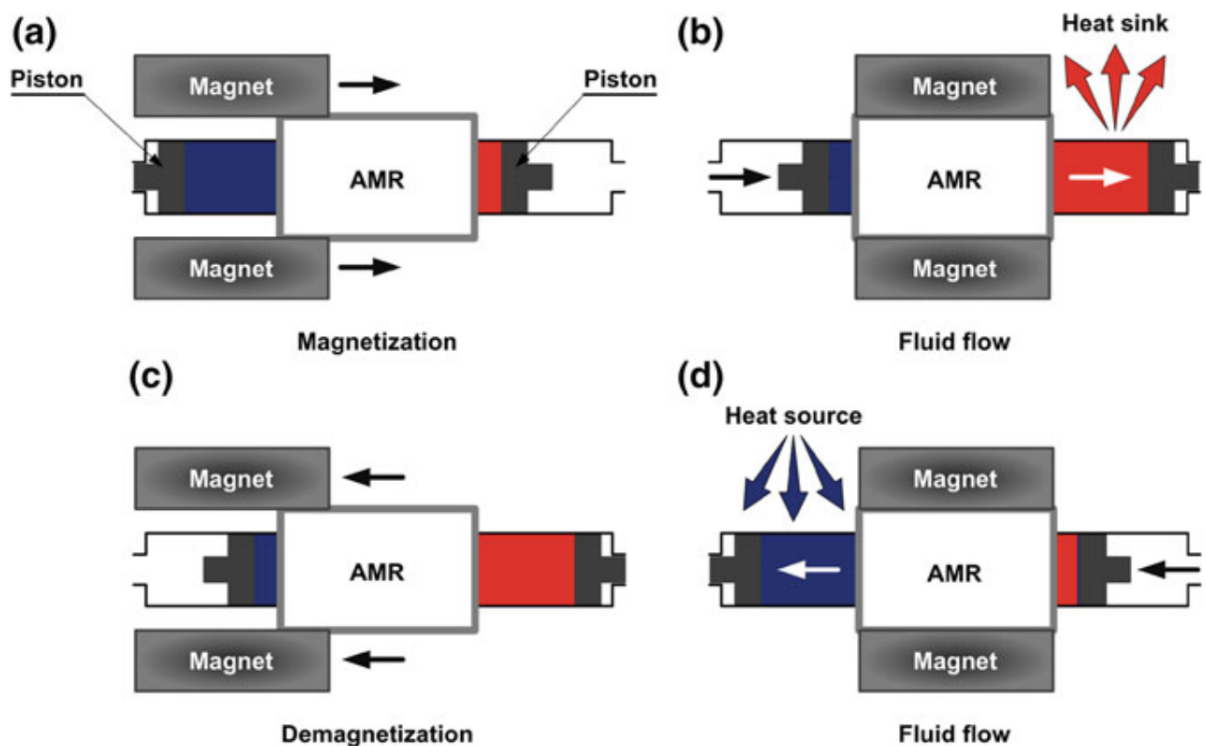


Figure 2.4: Schematic of four basic steps of Brayton-like AMR cycle in reciprocating device (picture taken from [9])

After some time, a periodic steady state is reached in which no further temperature change in the hot zone nor cold zone occurs in two successive cycles. A temperature profile then is established along the length of the AMR.

The regenerator can be formed in a parallel plate configuration (Fig. 2.5 b) or it has a porous structure. In this study, the latter will be the case. The porous structure can be

composed by the uniform spherical packed bed (Fig. 2.5 d). Performances of an AMRR can

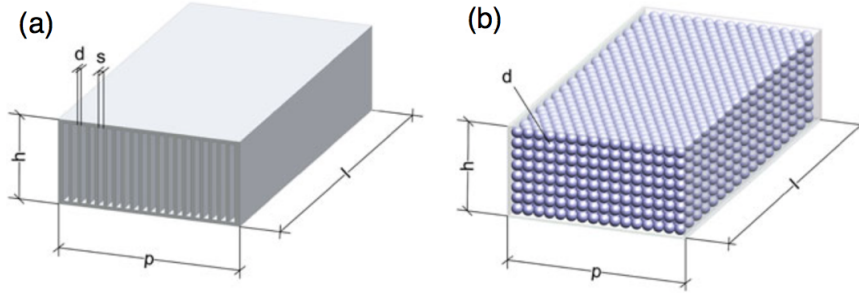


Figure 2.5: Schematic of four different AMR geometries (picture taken from [9])

be evaluated by its refrigeration capacity and its Coefficient of Performance (COP), which calculated by the following equations.

$$\dot{Q}_C = \dot{Q}_{ref} = f \int_0^{\tau_f} \dot{m}_f c_{p,f} (T_{f,c,in}(t) - T_{f,c,out}(t)) dt \quad (2.31)$$

$$\dot{Q}_H = \dot{Q}_{rej} = f \int_0^{\tau_f} \dot{m}_f c_{p,f} (T_{f,h,in}(t) - T_{f,h,out}(t)) dt \quad (2.32)$$

$$COP_{ref} = \frac{\dot{Q}_{ref}}{\dot{W}_{in}} = \frac{\dot{Q}_{ref}}{\dot{W}_{mag} + \dot{W}_{pump}} \quad (2.33)$$

For an ideal AMR system operating in a periodic steady-state condition, the magnetic work input (\dot{W}_{mag}) is equal to the difference between the cooling and heating power, mathematically expressed as:

$$\dot{W}_{mag} = \dot{Q}_H - \dot{Q}_C \quad (2.34)$$

Several reports regarding the modeling of the AMR with spherical packed bed are reviewed [17] [18] [19]. Things in common in those three models are: using Gd as MCM; one-dimensional; ideal (instantaneous) magnetic field change and mass flow rate (see Fig. 2.6); and apply direct method in the inclusion of the MCE. The model developed in this study has several differences in those things (further explained in Chapter 3).

The ideal (instantaneous change) of mass flow rate and magnetic field, with constant hot side temperature, gives a profile pictured by Fig. 2.7. As expected, the increase and decrease of the MCM temperature happen in an instant, which is not practical in the real situation.

The model needs data of magnetocaloric properties of MCM, namely Gd and MnFe(P,Si) compound. The measurement data is required to include the MCE to the model as a heat source term. The reports of [20] and [21] reveals that Gd and MnFe(P,Si) have different magnetocaloric characteristics. Gd is a second order material while MnFe(P,Si) compound is a first order material. An experimental study report of a packed-bed AMR is also needed as a reference to validate the model which further explained in Chapter 3.

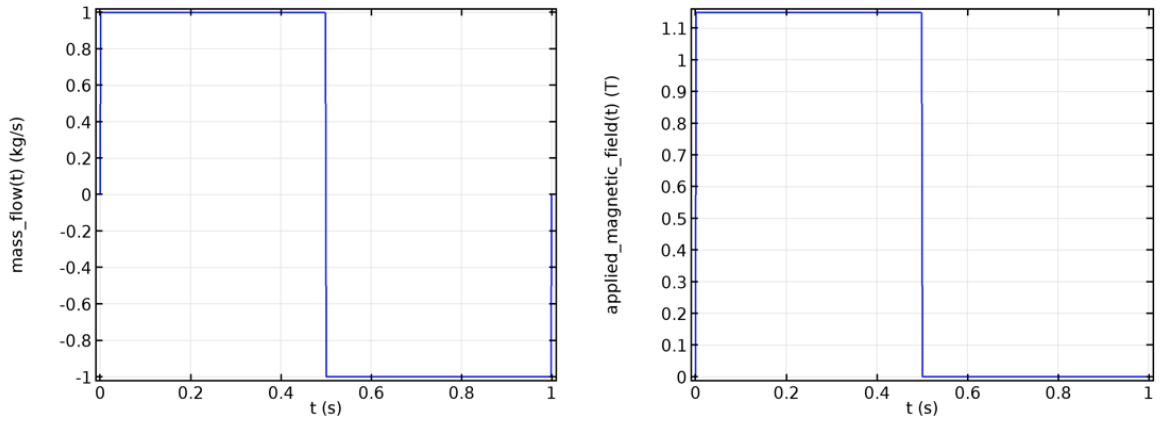


Figure 2.6: Instantaneous change in mass flow rate (left) and applied magnetic field (right) profile

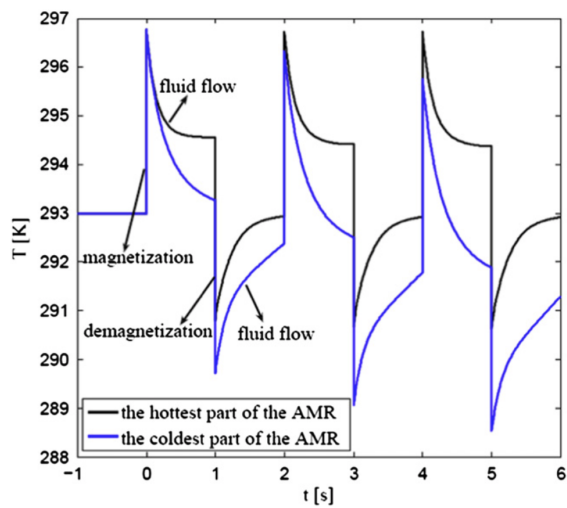


Figure 2.7: MCM temperature profile with instantaneous temperature change during the cycle (picture taken from [17])

Modeling and simulation

3.1 AMR geometry and operational parameter

The model is built based on the specifications mentioned in an experimental report of Tušek et. al., [12]. The results of this experimental study are used to verify the outcome from the model simulations. The work of [12] examine six different Gadolinium AMR configuration. One of the tested AMR is a packed-bed with spherical particles of 0.349 average porosity. The diameter of the particle is varied between 0.35 to 0.5 mm. The given results are includes the optimization of the temperature span (see: Fig. 3.1), refrigeration capacity, and COP (see Fig. 3.2). The important information regarding physical parameters of the AMR which used in the model is summarized in Table 3.1.

Table 3.1: AMR physical parameter

| Parameter | Symbol | Value | Unit |
|---------------------------------|---------------|--------|---------|
| length | L | 0.08 | m |
| width | W | 0.039 | m |
| height | H | 0.01 | m |
| average porosity | ε | 0.349 | - |
| sphere diameter | d_p | 0.0005 | m |
| mass of Gd | m_{Gd} | 0.135 | kg |
| maximum magnetic field strength | $\mu_0 H$ | 1.15 | $Tesla$ |

The model consists of the solid part made from spherical particles of magnetocaloric material (Gadolinium or the MnFe(P,Si) compound) and fluid part (the water-ethylene glycol solution) with porosity 0.349. The schematic of the model domain depicted in Fig. 3.3 shows that the model is assuming a thickness of the regenerator of 0.179 mm so that the ratio of void volume to the total available volume is equal to the porosity. The properties of the materials are taken from COMSOL library, except for the following:

- Density, thermal conductivity, and dynamic viscosity of the working fluid, a mixture of 70% water and 30% ethylene glycol, are taken from a published data sheet of commercial fluid [22].

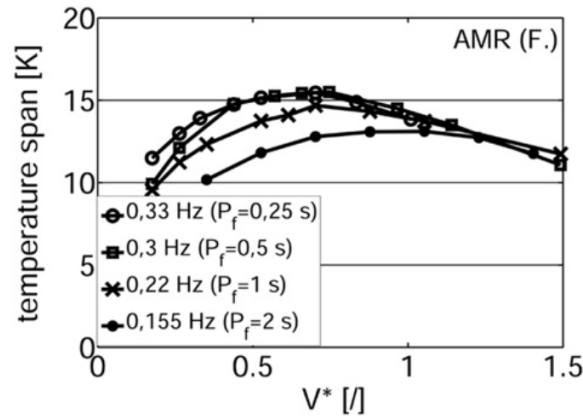


Figure 3.1: Temperature span as a function of the ratio of displaced fluid volume at different operating frequencies for the spherical packed-bed AMR (picture taken from [12])

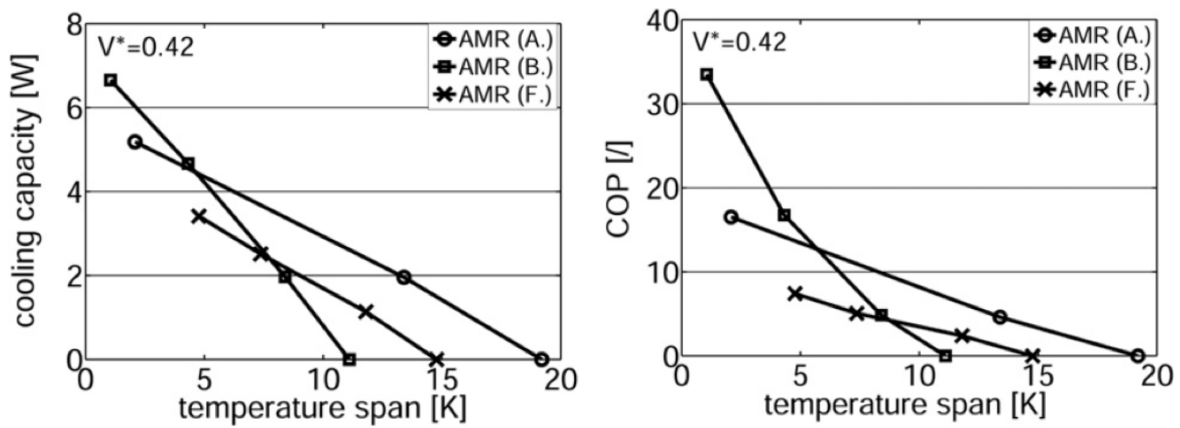


Figure 3.2: Cooling capacity (left) and COP (right) as function of T_{span} at f 0.3 Hz with V^* 0.42; AMR F is the one with spherical packed-bed AMR (picture taken from [12])

- Magnetization and specific heat for Gd are taken from the report of [20] which explained in the Section 3.4. The specific heat data at different temperature for a certain applied magnetic field is not available at COMSOL material library.
- The magnetocaloric properties data for MnFe(P,Si) compound is taken from [21] [23] [24], which further also explained in Section 3.4.

The experiment apparatus has some constraint to reach higher frequency, especially related to long (de)magnetization time (τ_{mag}), 0.75 s, and the dead time due to the delay of the electric actuator (piston pump) and the pneumatic cylinder (magnet assembly) control response. The dead time during one cycle is 0.9 s.

Refer to Fig. 3.1, the best result is obtained in operating frequency (f) 0.33 Hz with fluid flow periode (P_f) 0.25 s. Based on this information and the explanation from the previous paragraph, the profile of magnetic field change and mass flow rate of the experimental condition at f 0.33 Hz is pictured by Fig. 3.4. Please be aware that the profile has been normalized into dimensionless form, therefore the maximum value is equal to 1. The dead

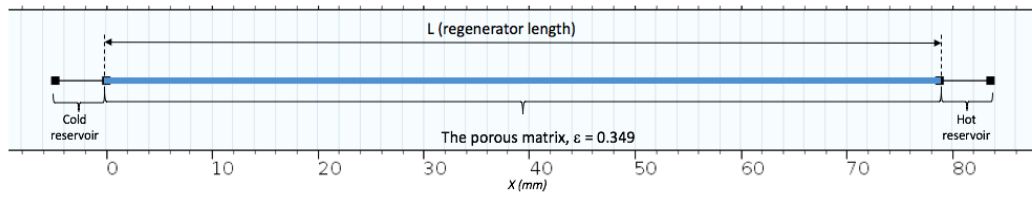


Figure 3.3: Sketch of the domain

time ($\tau_{dead-time}$) is divided into two parts, $\tau_{dead-time1}$ and $\tau_{dead-time2}$ with 0.45 s each. It is shown by the picture that the portion of dead time and (de)magnetization are very dominant, therefore the system cannot reach a higher frequency.

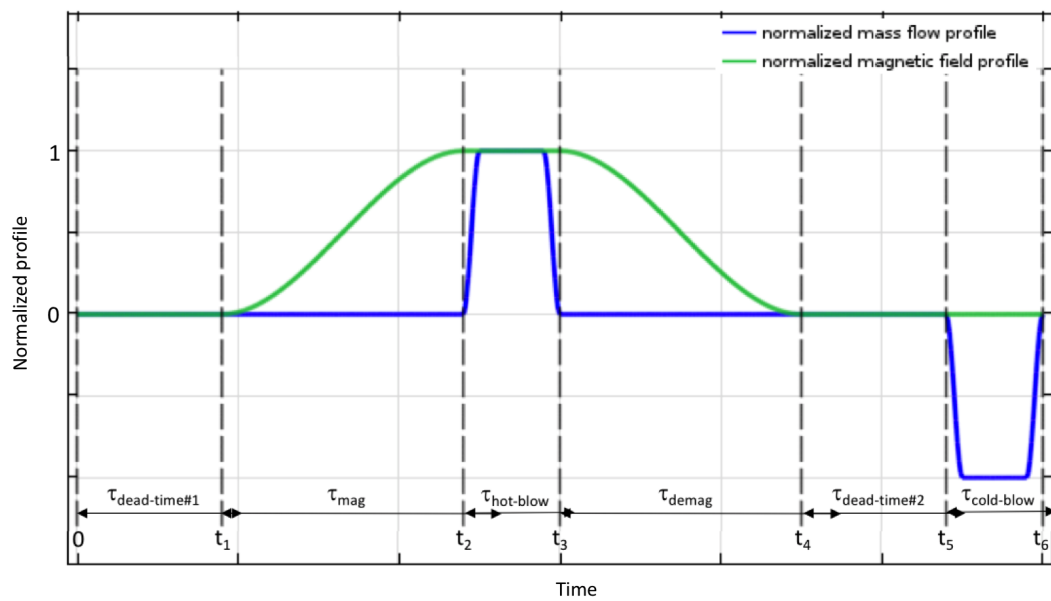


Figure 3.4: Profile of normalized fluid mass flow and applied magnetic field for one cycle

To simplify the problem, a set of assumptions is made in the mathematical model, as following:

- The fluid is incompressible
- No pressure oscillation
- The solid spherical particles are uniformly distributed in the AMR, hence no flow maldistribution
- The radiation heat transfer influence is neglected
- Ideal work of heat exchanger (Hot Heat Exchanger (HHEX) and Cold Heat Exchanger (CHEX))
- The applied magnetic field (in the empty air gap of the magnetic field source) is equal to the internal magnetic field in the MCM, which implies the demagnetization field is neglected.

Parasitic heat loss to the environment, with the measured environmental temperature of 22 °C, is included in the calculation based on the information from [25], in the form of thermal

resistance, 10 W/K for the AMR housing and 25 W/K for the cold reservoir. The apparatus also equipped with a heat exchanger on the hot side to fix the HHEX temperature to 27 °C.

3.2 Numerical setup

3.2.1 The governing equations

The set of governing equations solved by the software has been mentioned in Section 2.2, Eq. 2.24 and 2.25, as rewritten by Eq. 3.1 and 3.2. COMSOL couples both of the governing equations and put into account all the equations related to heat transfer in porous media (as explained by Section 2.2) by specifying the average radius of the spherical pellet bed.

$$(1 - \varepsilon)\rho_s c_{p,s} \frac{\partial T}{\partial t} = (1 - \varepsilon)k_s \frac{\partial^2 T}{\partial x^2} + h(a_{sf})(T_f - T_s) + \dot{Q}_{MCE} \quad (3.1)$$

$$\varepsilon\rho_f c_{p,f} \frac{\partial T}{\partial t} + \varepsilon\rho_f c_{p,f} u_D \frac{\partial T}{\partial x} = \varepsilon k_f \frac{\partial^2 T}{\partial x^2} + h(a_{sf})(T_s - T_f) \quad (3.2)$$

3.2.2 The boundary conditions

Refer to equation 2.25 and 2.24, three boundary conditions are required: one initial condition and two spatial boundary conditions. The initial temperature is defined. As mentioned in Section 3.1, the HHEX temperature is fixed to 27 °C. The solid and fluid at the end of a fluid flow step in a cycle (means that in every half a cycle), will be the initial condition for the next half a cycle. Therefore, the boundary conditions are complete, which mathematically expressed as:

$$T(x = 0, t) = T_c; \quad \left. \frac{\partial T}{\partial x} \right|_{L,t} = 0 \quad (\text{during hot blow}) \quad (3.3)$$

$$T(x = L, t) = T_h; \quad \left. \frac{\partial T}{\partial x} \right|_{0,t} = 0 \quad (\text{during cold blow}) \quad (3.4)$$

3.2.3 Mesh characteristics

The Fourier number (Fo) criterion is applied to fulfill the stability requirement. As a common rule of thumb, the Fo should be less than 1 on all domains. It implies that the thermal penetration during a single time step is less than one grid cell. The Fo is calculated based on Eq. 3.5, which one can consider that applying small mesh size requires small timestep; but a large mesh possibly leads to an inaccurate result.

$$Fo = \frac{\alpha \Delta t}{\Delta x^2} \quad (3.5)$$

$$\alpha = \frac{k}{\rho c_p} \quad (3.6)$$

The mesh size is determined by considering the size of the smallest entity in the domain, in this case is the spherical particle radius (r_p). With the maximum mesh size of $r_p/2$, the corresponding time step size is at most 0.0025 s. With this sizes, the maximum Fo is 0.92 for the solid and 0.019 for the fluid.

3.3 Improving the operational setup configuration

As also acknowledged by the author in [12] [16], the weakness of the experimental setup is due to the high τ_{mag} , hence the ratio of τ_{mag}/P_f is too high: $0.75/0.25=3$. According to Plaznik et. al. [16], the dead time can be decreased to 0.2 s (from 0.9 s). In addition, in a Brayton-like cycle with lower operating frequency for τ_{mag}/P_f ratios between 0.125 and 1, it has considerably equal performances, in terms of cooling capacity and COP.

The existence of dead time and a slow τ_{mag} is preventing the system to reach higher operating frequency. Therefore, the improvement to the operational parameter is based on changes to the τ_{mag} from 0.75 s to 0.25 s and eliminating the dead time. The corresponding profile of the \dot{m}_f and $\mu_0 H$ as the function of time is shown in Fig. 3.5.

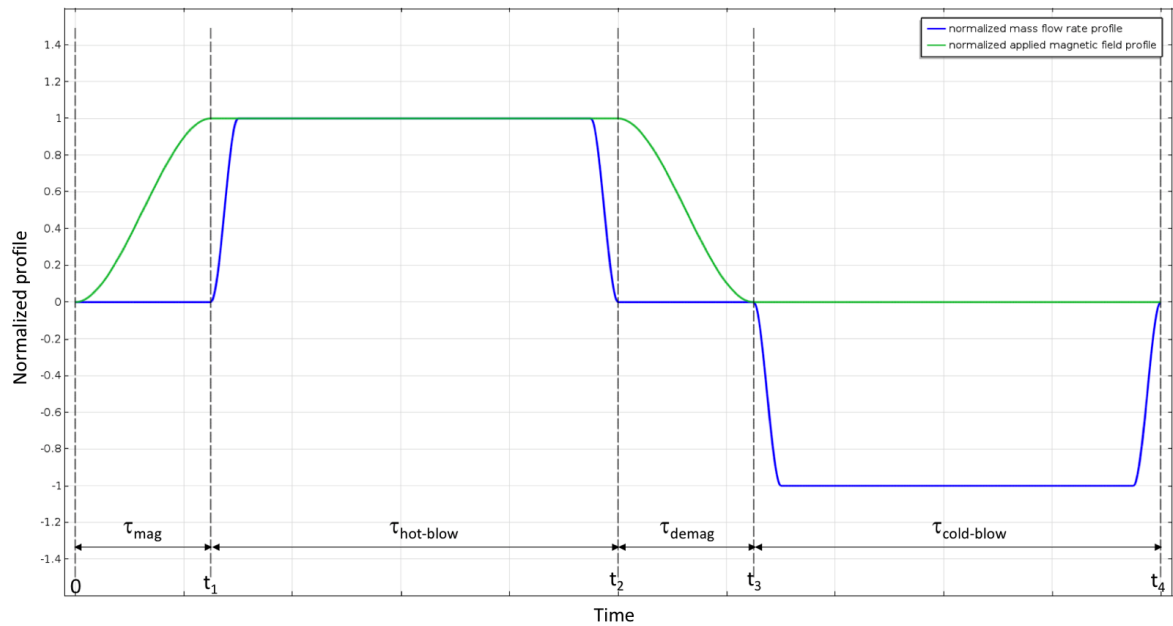


Figure 3.5: Profile of the applied magnetic field and the mass flow rate with t_{mag} 0.25 s and frequency 0.5 Hz for one cycle

An operational parameter variation is done by changing the f (0.5 Hz, 1 Hz, and 1.25 Hz) and mass flow rate of the working fluid (\dot{m}_f). The displaced fluid ratio (V^*) is introduced and used to compare the performances in different operational parameters, which are calculated with the following equations.

$$V^* = \frac{\dot{m}_f \tau_f}{\rho_f V_{AMR} \epsilon} \quad (3.7)$$

3.4 Inclusion of MCE

3.4.1 Gadolinium

The MCE is included to the model via the heat source term (\dot{Q}_{MCE}) refer to equation 2.14, which needs informations of the magnetization (M) as function of temperature (T) and applied magnetic field ($\mu_0 H$). The similar method is also done by the previous master thesis assignment [5] [26].

Data $M(T, \mu_0 H)$ for Gd is taken from the report of Dan'kov [20] which gives the magneto-thermal properties of four different samples of Gd (with different purities). The magnetocaloric effect to the material is studied by three experimental techniques direct measurements of the adiabatic temperature rise, magnetization, and heat capacity.

Fig. 3.6 depict the corresponding data of magnetization and heat capacity as the function of T and $\mu_0 H$. It observed that the T_{curie} of Gd is around 293 K. The data is accurate but interpolation is necessary since the applied magnetic field change used in the study is between zero to 1.15 T. One can notice from Fig. 3.6 that the available heat capacity data is jumping from 0 T to 2 T. The figures also tells that Gd is a MCM with Second Order Magnetic Transition (SOMT) characteristics (please refer to Fig. 1.3)

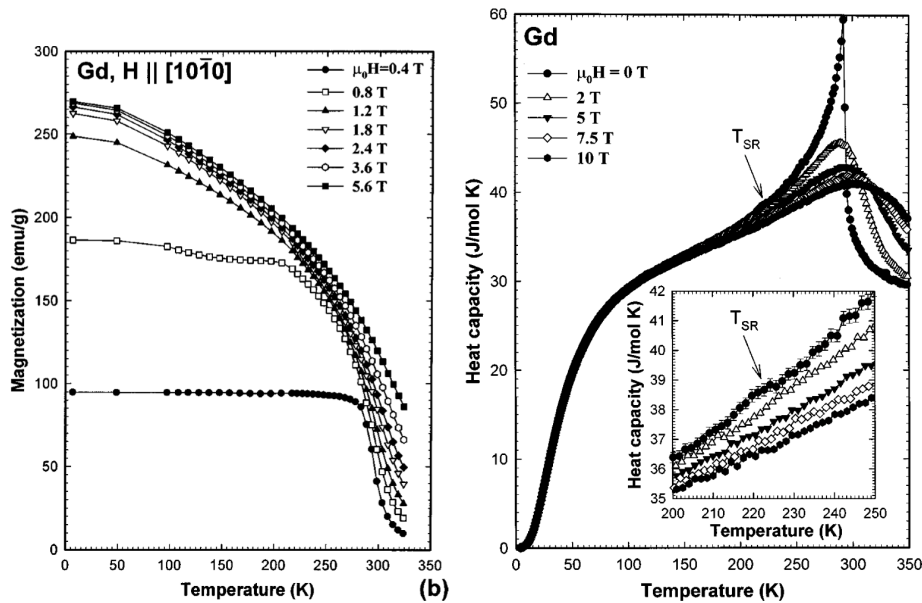


Figure 3.6: Magnetocaloric properties data of Gd from Dan'kov and Tishin. Left: Magnetization (emu/g is equivalent to Am^2/kg); right: heat capacity with molar mass of Gd is $157.25 g/mol$ (picture taken from [20])

The visualization of the synthesized data from Fig. 3.6 with linear interpolation is shown by Fig. 3.7 for $M(T, \mu_0 H)$ and Fig. 3.8 for $C_p(T, \mu_0 H)$.

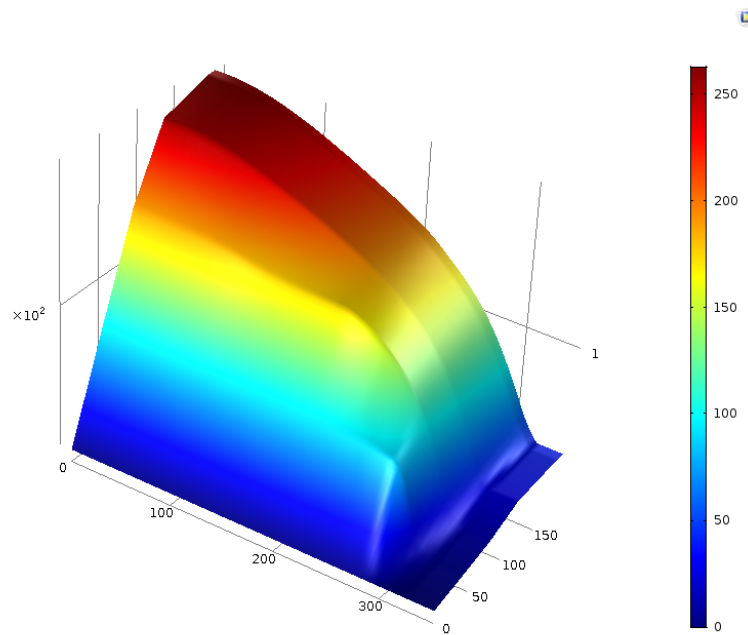


Figure 3.7: Magnetization of Gd as function of T and $\mu_0 H$

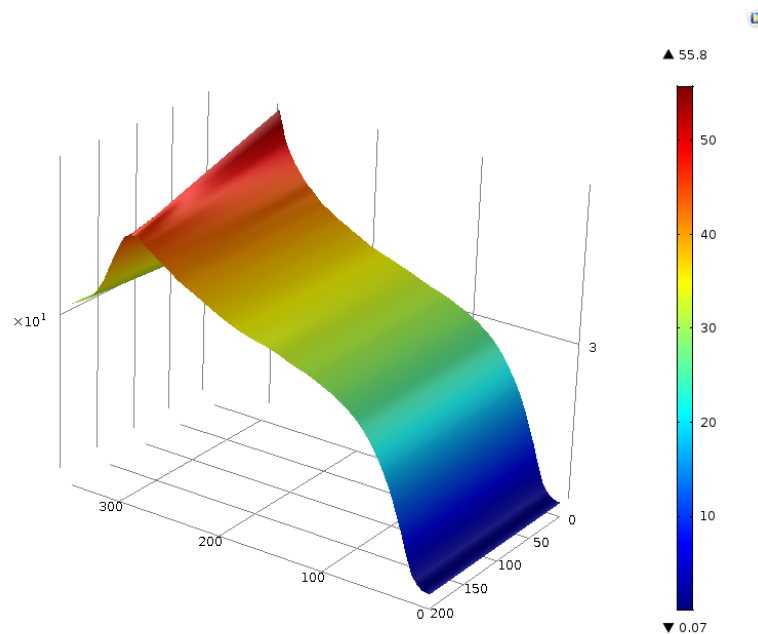


Figure 3.8: Visualization of heat capacity as function of temperature and magnetic field strength

3.4.2 The MnFe(P,X) compound

The magnetocaloric properties data of the MnFe(P,X) compound are obtained from the report of Yibole, et. al. [21]. The report gives the result of an experimental investigation of the magnetocaloric properties of the MnFe(P,X) ($X = \text{As}, \text{Ge}, \text{Si}$) materials. The previous developed well-performed arsenic (*As*)-based is not favorable due to its toxicity. The cheap and safe alternatives to MnFe(P,X) ($X = \text{As}$ or Ge) MCM led to the discovery of the third generation compound, the silicon-based.

The MnFe(P,Si) type had excellent MCE properties and became a promising candidate as refrigerants in magnetic refrigeration. The Si-based $\text{Mn}_{1.25}\text{Fe}_{0.7}\text{P}_{0.49}\text{Si}_{0.51}$ has T_{curie} around room temperature makes it a potential alternative. However, this material has a limitation in its optimum operational temperature range.

Fig. 3.9 shows the data of Magnetization as a function of temperature and magnetic fields. One can notice that there are differences in magnetocaloric characteristics between Gd and the MnFe(P,Si) compound. In Gd, for an applied magnetic field larger than 0.8 T, significant change of internal magnetization (slope of the magnetization curve as shown in Fig. 3.6) occurs in wide temperature range, from 50 to 330 K. On the other hand, $\text{Mn}_{1.25}\text{Fe}_{0.7}\text{P}_{0.49}\text{Si}_{0.51}$ only provides the slope in a narrow range from 280 to 310 K. The situation leads to an idea of the application of layered AMR with different Curie temperature.

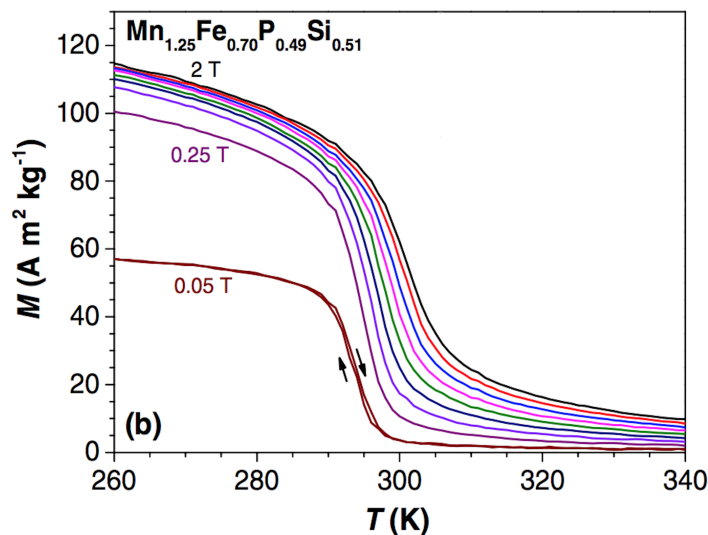


Figure 3.9: Magnetization as function of temperature of $\text{Mn}_{1.25}\text{Fe}_{0.7}\text{P}_{0.49}\text{Si}_{0.51}$ at 0.05 T and 0.25 T to 2 T (picture taken from [21])

As noticed from Fig. 3.9, the value of $\frac{dM}{dT}$ is high only in a narrow range of temperature, which makes the layered AMR application necessary. Fig. 3.10 visualize the magnetization as a function of temperature and applied magnetic field which includes to the model.

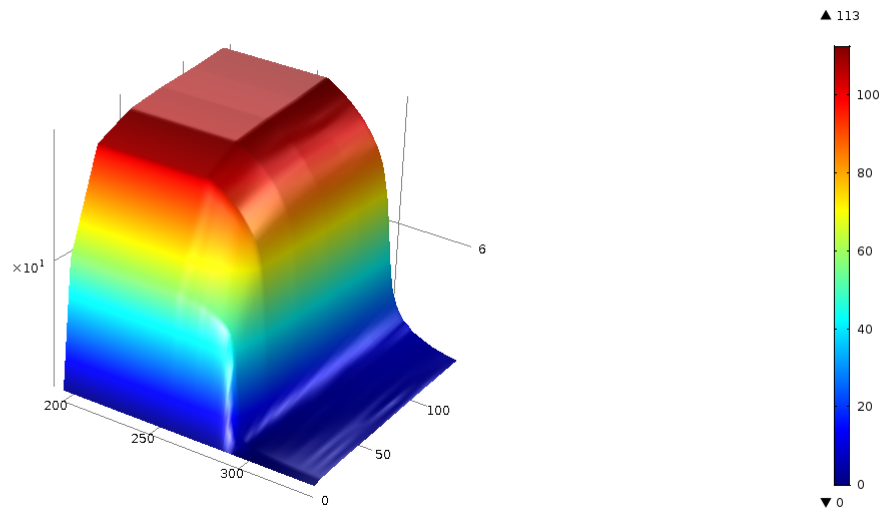


Figure 3.10: Magnetization of $Mn_{1.25}Fe_{0.7}P_{0.49}Si_{0.51}$ as function of T and $\mu_0 H$

3.5 The layered AMR

The primary objective of a layered AMR configuration is to optimize the system performance, concerning the fact that there is a difference of magnetocaloric characteristics of Gd and MnFe(P,Si) compounds. The distinction is indicated by the magnetization profile as shown in the previous section (see Fig. 3.6 and 3.9). Referring to the schematic curve in Fig. 1.3, one can notice that Gd is a second order material, while MnFe(P, Si) compound is a first order.

A first order MCM has an excellent MCE only in a narrow temperature range. Therefore a layered AMR configuration is an alternative solution to make the AMR works well in a wider temperature range. The layer applied in the model consist of $Mn_{1.25}Fe_{0.7}(P_{1-y}Si_y)$ compound with four different y values; 0.49, 0.50, 0.51, and 0.52 as depicted by Fig. 3.11. Higher y values correspond to higher T_{curie} , therefore the compound with $y = 0.49$ is placed close to the cold end and the $y = 0.52$ is at the other end.

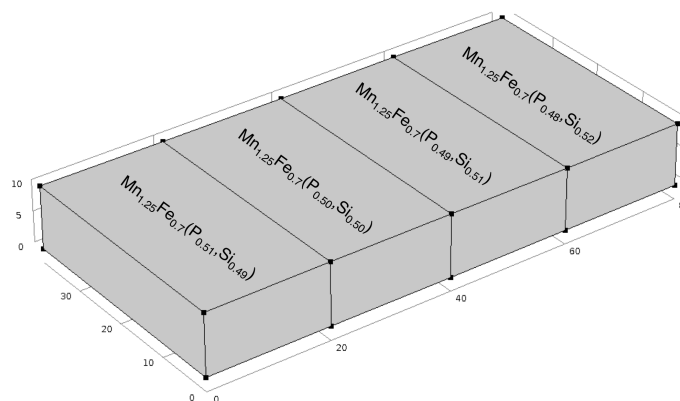


Figure 3.11: Schematic configuration of the layered AMR

Report of [21] does not give all the necessary information of the magnetization as a function of temperature for a various applied magnetic field for every y values. The report of [21] presents magnetization data at a various applied magnetic field for $Mn_{1.25}Fe_{0.7}P_{0.49}Si_{0.51}$. For other y values, only data at 1 Tesla is given.

The lack of data is tackled by a projection, meaning that the behavior of $M(T)$ for every y values for various applied magnetic field is proportional to that in $y = 0.51$ (see Fig. 3.10). The data of $Mn_{1.25}Fe_{0.7}P_{0.49}Si_{0.51}$ is projected to other y values by changing the temperature based on the temperature at 1 Tesla. Fig. 3.12 shows the data of $M(T, \mu_0 H)$ for the compound with y value 0.49, 0.50, 0.51, and 0.52. Therefore, the shape of the $M(T, \mu_0 H)$ curve for other y values are identical (proportional) with Fig. 3.10 but at different T_{curie} . Referring to [21], the higher P/Si ratio triggers T_{curie} to become lower and promote the thermal hysteresis as also indicated by Fig. 3.12.

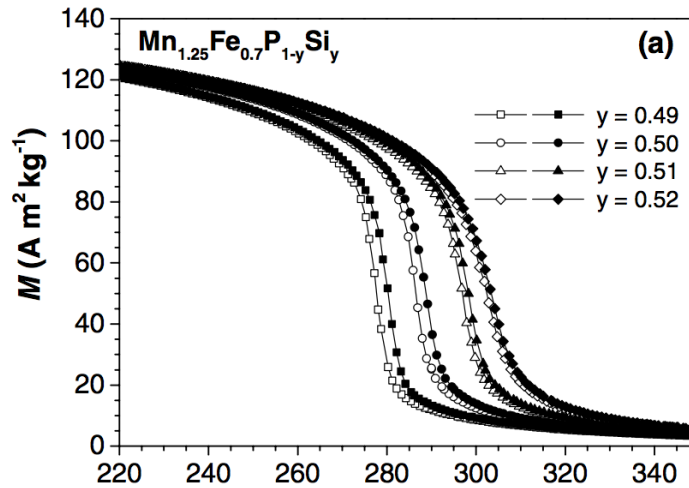


Figure 3.12: Magnetization curves during heating (closed symbols) and cooling (open symbols) for the $Mn_{1.25}Fe_{0.7}P_{1-y}Si_y$ at 1 Tesla (picture taken from [21])

The model also assumes that the hysteresis effect to the magnetization is neglected by taking the middle value between the heating curve and the cooling curve.

Other property data needed for the simulation are density, thermal conductivity, and heat capacity. The report of [27] provides data of density and thermal conductivity that is 5500 kg/m^3 and 3.5 W/mK , respectively. The density and the thermal conductivity are assumed to be constant, not dependent on temperature and applied magnetic field. The report also mentions that the heat capacity for the $MnFe(P,Si)$ compound is around 1500 J/(kg.K) . However, for heat capacity, this information is not sufficient.

Similar situation to the magnetization data, a complete data of heat capacity as a function of temperature and applied magnetic field is not successfully found during the process of this thesis. Therefore, to complete the data, the approach is taken by taking the heat capacity data of the $MnFe(P,As)$ compound which is provided by [28] as the reference. Fig. 3.13 shows the estimated heat capacity that includes to the model which neglecting the hysteresis between cooling and heating. The complete data on the magnetization and the heat capacity as a function of temperature at a various applied magnetic field is given in the Appendix.

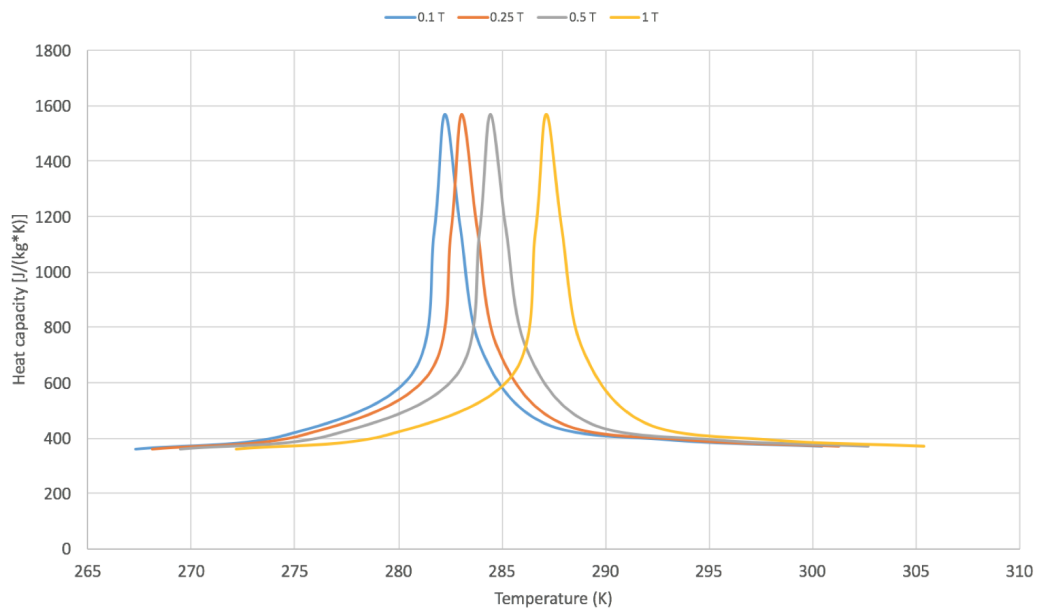


Figure 3.13: The estimated heat capacity for the compound with y 0.50 at various applied magnetic field

There are consequences from applying this projection method. One might deem that the projected data is not accurate. Chapter 4 discuss the related implications of this approach to the magnetocaloric effect of the compound.

Result and discussion

The identification and naming are introduced to ease the explanation. The spherical MCM particles, either Gd or the MnFe(P,Si) compound, may also be referred as "the solid." Accordingly, "the fluid" refers to the water-ethylene glycol solution working fluid. The model developed in this thesis is used to run three groups of simulation namely:

1. The original experimental apparatus according to [12], which uses Gd as MCM and contains 0.9 s dead time and 0.75 s τ_{mag} . This simulation is mainly aimed to validate the models that have been made.
2. The optimized Gadolinium AMR by eliminating dead time and shortening τ_{mag} to 0.25 s, with its variation of operational parameters (f and \dot{m}_f).
3. The optimized model with four layers of MnFe(P,Si) compound as MCM.

4.1 Validation of the model

4.1.1 The MCE in Gadolinium AMR model

Prior to the complete simulation involving heat transfer with the working fluid, it is important to see the implementation of MCE in the model. As explained, the MCE is integrated to the model as a heat source. The amount of heat is proportional to the first derivative of internal magnetization with respect to temperature, dM/dT , (see 2.14). The $M(T, \mu_0 H)$ and $C_p(T, \mu_0 H)$ are taken from [20], as explained in Chapter 3.

Please also recall the time identification as depicted in Fig. 3.4, which consist of:

- t_0-t_1 : dead time 1 ($\tau_{dead-time1}$)
- t_1-t_2 : magnetization (τ_{mag})
- t_2-t_3 : hot blow ($\tau_{hot-blow}$)
- t_3-t_4 : demagnetization (τ_{demag})
- t_4-t_5 : dead time 2 ($\tau_{dead-time2}$)
- t_5-t_6 : cold blow ($\tau_{cold-blow}$)

Fig. 4.1 shows the response of the MCM in the form of temperature change, increase and decrease, as the magnetic field moves in and moves out from the MCM. The model gives an acceptable prediction of the ΔT_{ad} of around 3.35 K for the applied magnetic field change from 0 to 1.15 T.

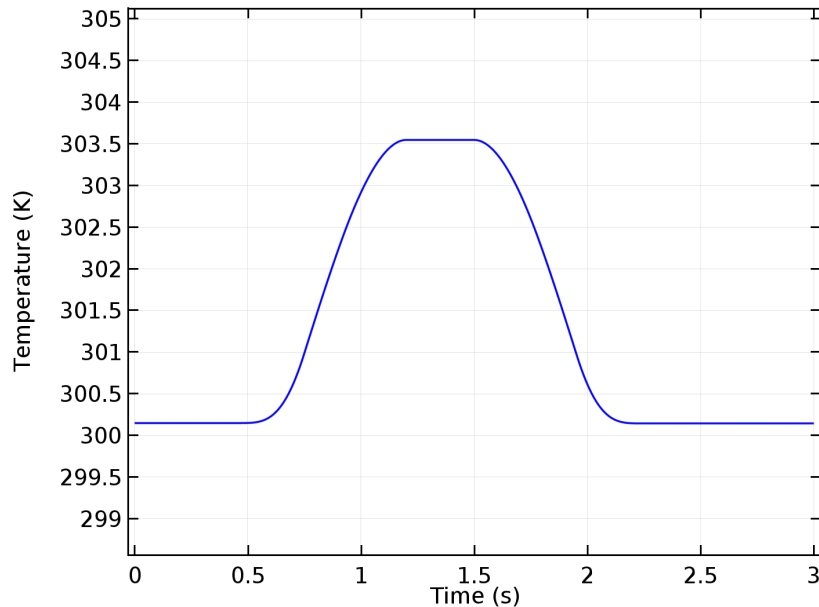


Figure 4.1: Adiabatic temperature change as given by the simulation for MCM Gadolinium with lower and higher $\mu_0 H$ 0 and 1.15 Tesla, respectively

The heat that goes into the AMR has to be reflected by an increase in the internal energy, or in other words; the heat source has to be equal to the change in internal energy. It is necessary to challenge this energy conservation to the model to see if the first law holds. Fig 4.2 (left) depicts the calculated heat source due to MCE. The graph on the right gives an idea on the deviation of the internal energy change to the MCE heat source. The source is only active during (de)magnetization because there are changes in the applied magnetic field. During constant field ($dH/dt=0$) the source no longer exists.

Fig. 4.2 indicates that there are discrepancies of the balance. It might be caused by the interpolation of magnetization and heat capacity data taken from [20]. The deviation is significantly less if the model uses heat capacity data at zero Tesla (C_p is only dependent on temperature) by directly using data from COMSOL material library for Gadolinium. As pictured in Fig. 4.3, the deviation is much less. The reason is that COMSOL does not incorporate the heat capacity dependency on the applied magnetic field change to the calculation. The discrepancy indicates a thermodynamic inconsistency; therefore the comparison of the simulation to an experimental result is very much needed for validation, which is further discussed in Section 4.1.3.

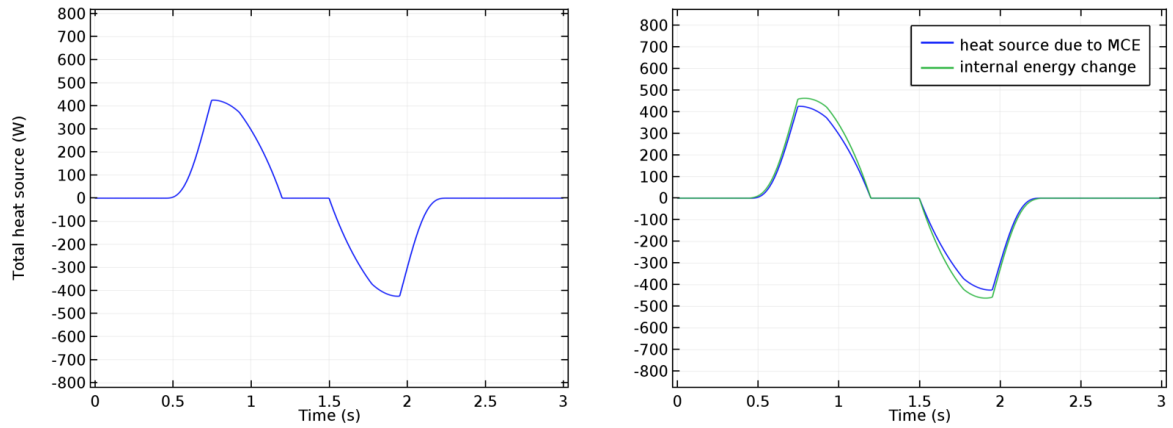


Figure 4.2: Heat source due to magnetocaloric effect for Gd in the model at initial temperature 27 °C (left). The MCE heat source compared to the change of internal energy (right)

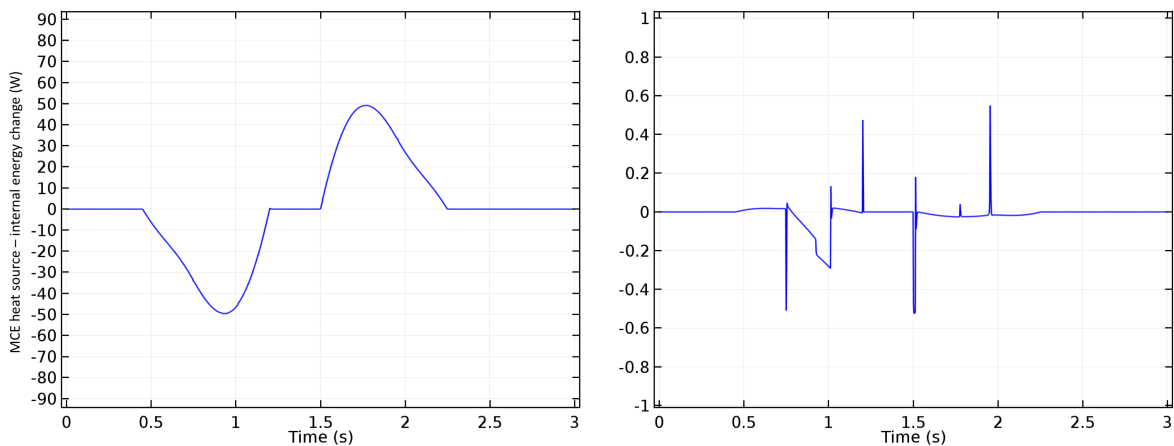


Figure 4.3: The deviation in energy balance due to interpolation of heat capacity data from [20] (left). Deviation is much less with heat capacity independent from the applied magnetic field change (right)

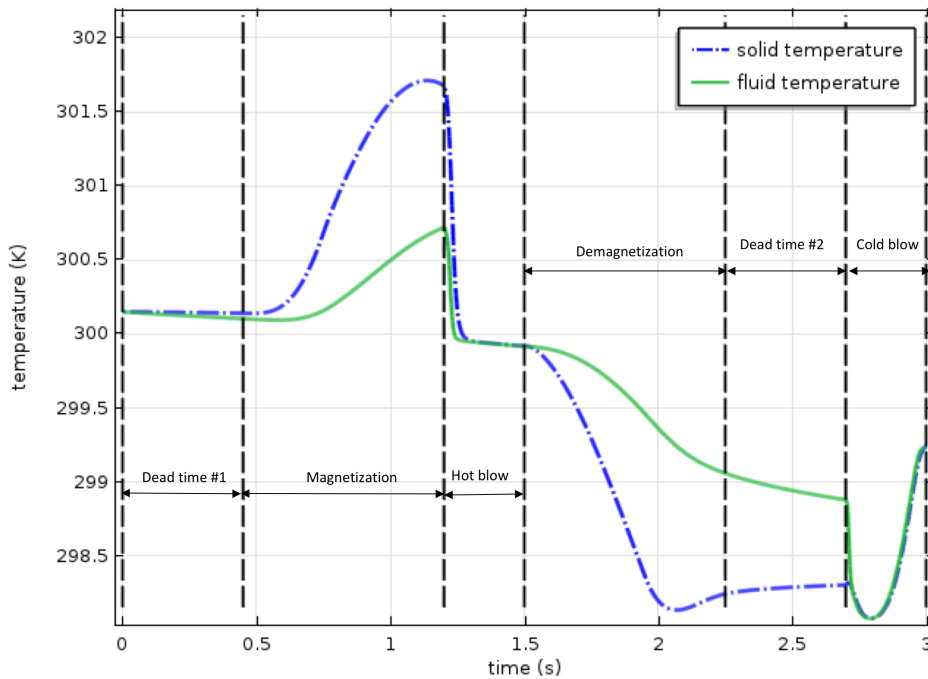


Figure 4.4: Temperature of the solid and the fluid at cold end of AMR for the first operational cycle at 0.33 Hz and $V^* 0.45$

4.1.2 Zero cooling load simulation

One cycle of the Brayton-like AMRR consist of four main steps: magnetization, fluid flow (hot blow) at constant maximum applied magnetic field (1.15 T), demagnetization, and cold blow at a lower magnetic field (zero Tesla). Fig. 4.4 pictures the temperature development of the fluid and the solid in AMR during this cycle. Since the hot heat exchanger temperature is fixed at 27 °C, the point of interest is the cold side.

It can be seen that the temperature during dead time is slightly decreasing due to parasitic heat loss to the environment. Please recall that at the initial condition, the temperature of the system is 27 °C while the environment is 22 °C. The fluid also starts to become hotter during magnetization and colder during demagnetization, although the fluid is not flowing yet. It happens due to heat conduction from and to the solid MCM which started to become hotter or colder 0.75 s of (de)magnetization, which makes the temperature increment not as high as the one shown in Fig. 4.1.

The solid-fluid temperature converges to a similar temperature a moment after hot blow started, and it is already lower than the initial temperature. The temperature continues to decrease in the demagnetization step, in which the conduction also occurs as in the magnetization step. The conduction continues during the second dead time since there is a noticeable temperature difference between the solid and the fluid. Finally, the solid-fluid temperature curve meets a moment after the cold blow starts. The solid-fluid temperature is decreasing in first one-third of cold blow period, due to the colder fluid near the cold end that flows into the cold end. It becomes colder than the cold end because of heat conduction to the demagnetized MCM due to long magnetization time.

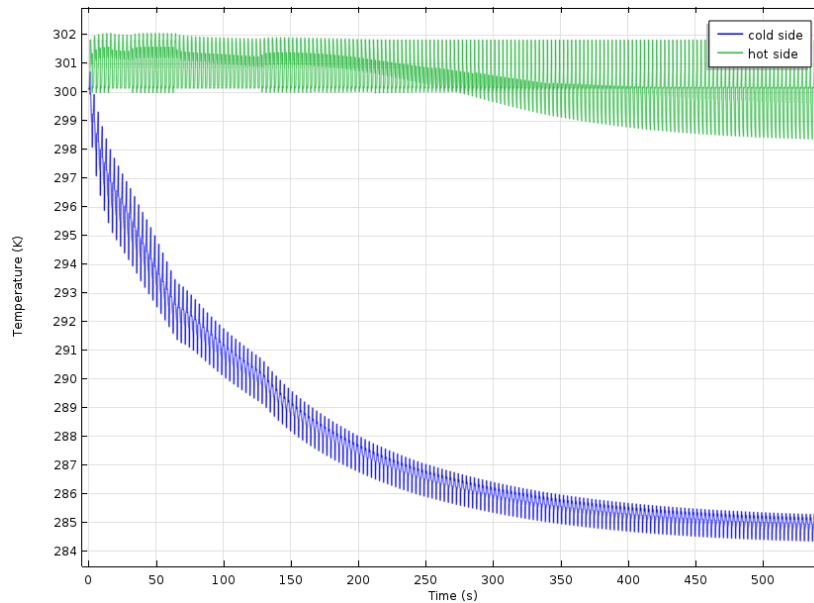


Figure 4.5: The temperature development that creates the temperature span between the hot end to the cold end for experimental device model at 0.33 Hz $V^* 0.45$

That is why we have an optimum point of V^* to obtain the maximum temperature span between the hot and the cold side of the AMR. If too much fluid from the cold side of the AMR arrives at the hot side (V^* close or larger than 1), the temperature span at the end will not be optimum. On the other hand, if the V^* is too low, the optimum temperature difference will not be reached either.

The periodic steady state is attained when the temperature at the end of the cold blow is the same as the temperature before the first dead time (the initial condition at next cycle). It took more than 500 seconds to obtain the periodic steady state, as depicted in Fig. 4.5 which shows the creation of the temperature span. The time is getting lower if the mass flow rate increase.

At periodic steady state, a temperature profile is established along the AMR length as shown in Fig. 4.6. It is also evident that the dead time does not have any significant influence on the system since the curve of temperature at the end of first dead time coincides with the initial curve as well as the second dead time with the temperature curve at the end of demagnetization. Therefore dead time is completely taken out in the next simulation with the optimized operational parameter.

The long τ_{mag} also is disadvantageous to the system, as indicated by Fig. 4.7 which shows a slow temperature increase (or decrease) rate. In the last 0.25 s of demagnetization, the temperature decrease even no longer exists. One can also see that heat transfer between MCM and working fluid is less effective by conduction (during (de)magnetization, at which the fluid is not flowing) compared to convection (during hot blow and cold blow). Therefore, cutting down the τ_{mag} is also done and applied in the next simulation to enhance the performance.

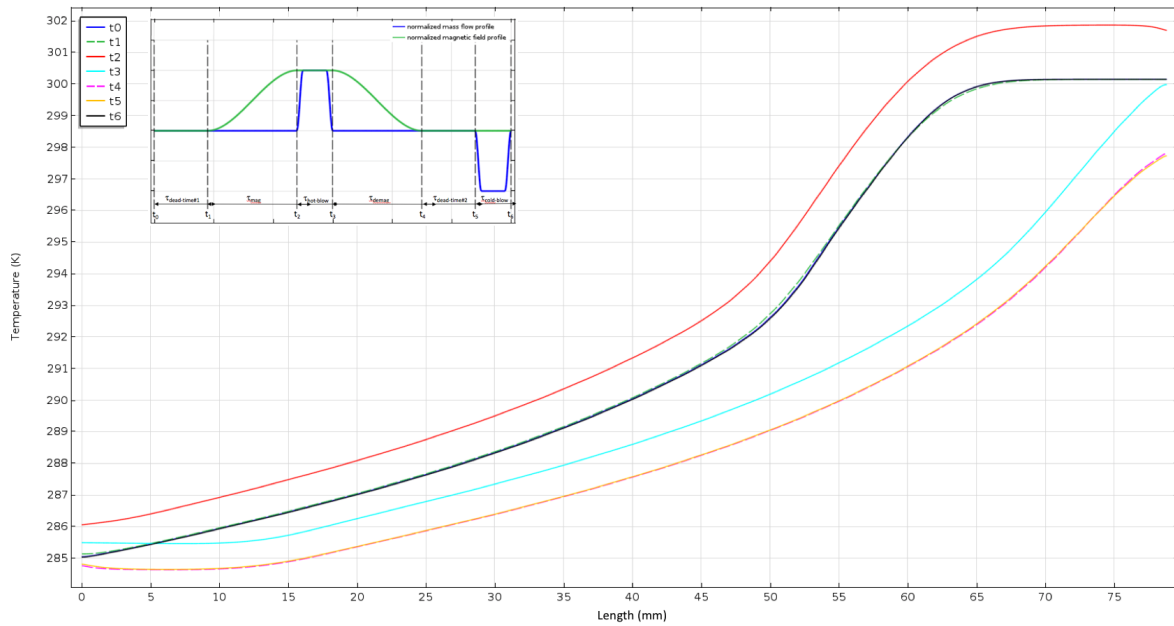


Figure 4.6: Temperature profile of the MCM along the AMR length after periodic steady state (f 0.33 Hz, V^* 0.45)

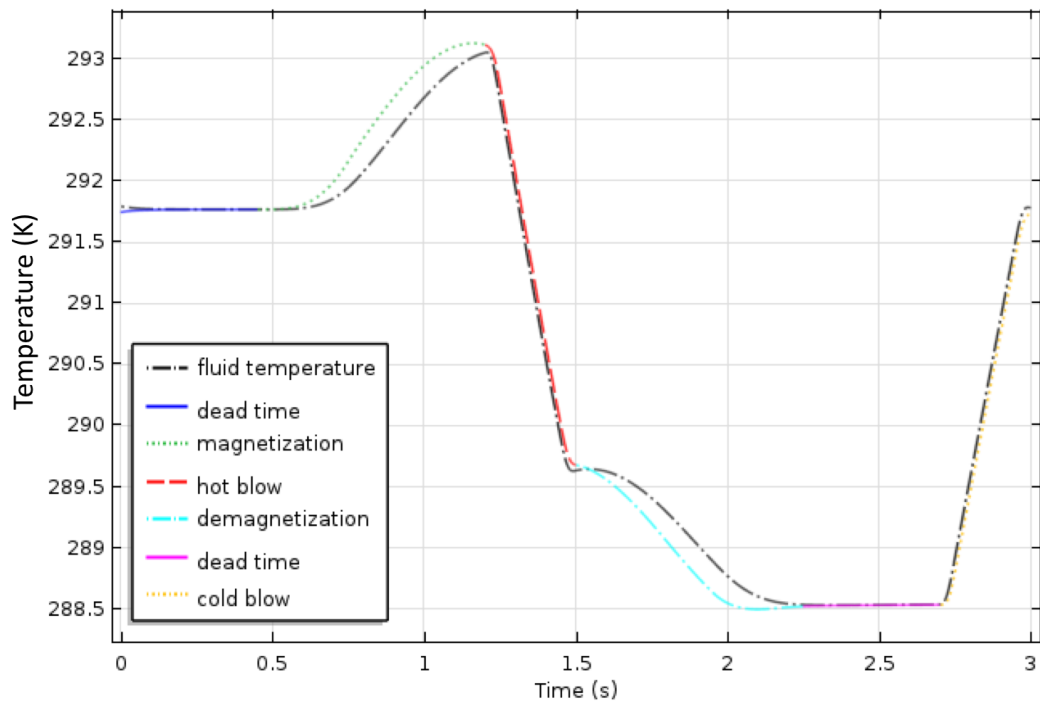


Figure 4.7: Average temperature profile of the MCM and the working fluid in every cycle step after periodic steady state (f 0.33 Hz, V^* 0.45). The dashed black line is the fluid temperature

Each particle of the MCM along the AMR has its own thermodynamic cycle because of the different temperature, following the profile in Fig. 4.6. The T-s diagram can be generated as depicted in Fig. 4.8. The T-s cycle surface is the largest for a material particle operating around the T_{curie} , which corresponds to the widest temperature difference created by the MCE. It is also noticed that (de)magnetization does not occur under adiabatic nor isentropic circumstances since there are changes in entropy, related to heat which is transferred to the quiescent working fluid and the parasitic heat loss which is included in the model.

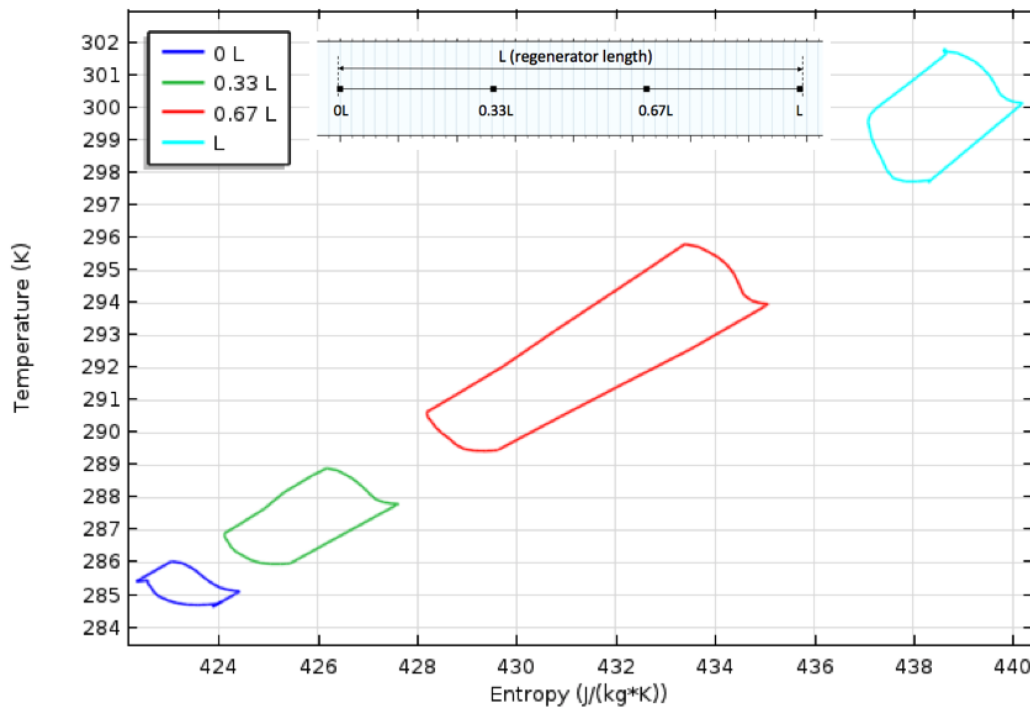


Figure 4.8: T-s diagram of the Gd solid refrigerant (MCM) at four different locations along the AMR length in one periodic steady state cycle (f 0.33 Hz, V^* 0.45)

4.1.3 Comparison of the temperature span

The results obtained from simulations are compared to the experimental results to verify its validity. Using the report of Tušek et. al [12] as the reference (see Fig. 3.1), a comparison is made of the temperature span as a function of V^* in Fig. 4.9 for operating frequency, f , 0.33 Hz. 0.33 Hz is chosen for the model verification since it gave the highest temperature span from the experiment, slightly higher than f 0.3 Hz. T_{span} is the fluid temperature difference at the hot reservoir (which is maintained at 27 °C) to the average fluid temperature at the cold end.

The result from the model is in good agreement with the experiment, especially for a lower value of V^* . It is also noticed that the maximum temperature span (T_{span}) is obtained at a similar value of V^* , around 0.75 for both results. The simulation gradually overestimates T_{span} (at zero cooling power) as V^* is increasing (hence the \dot{m}_f is also increasing). This

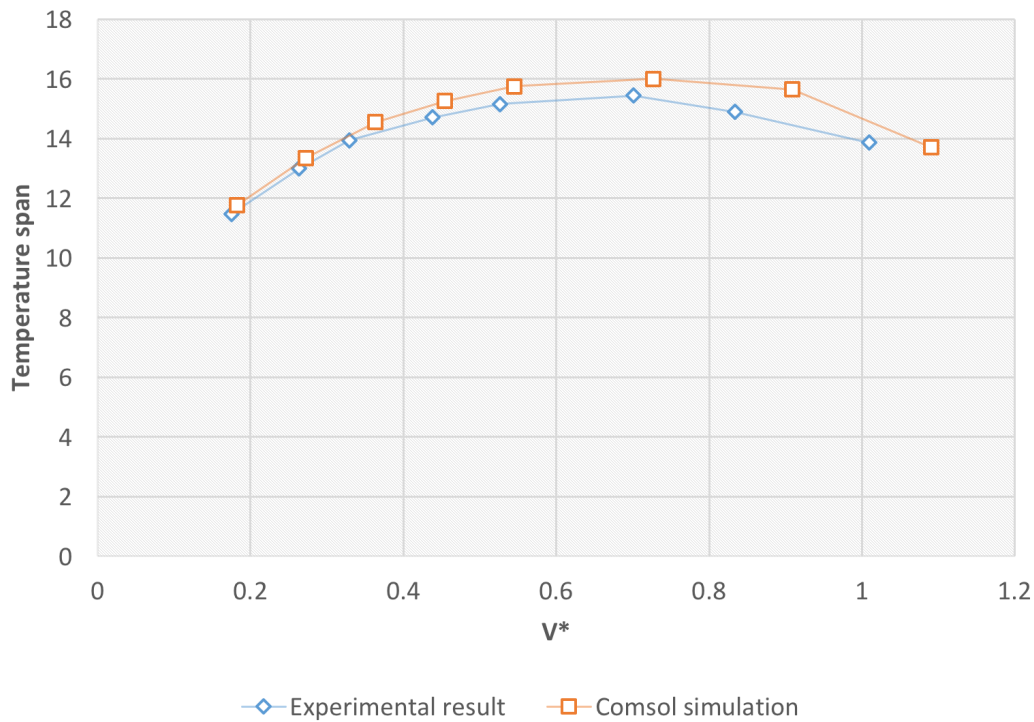


Figure 4.9: Comparison of experimental and simulation results for temperature span vs. V^*

might be caused by the fact that flow maldistribution losses are not included in the model, where the losses from maldistribution of flow are getting bigger for higher \dot{m}_f . Although deviated, it still has the same curve fashion.

In the actual condition, a packed-bed typically has a greater porosity near the wall compared to the middle, this makes the flow not uniformly distributed which also influences the fluid temperature. Also, the size (diameter) of spherical particles in packed-bed AMR of the experimental device varies from 0.35 to 0.5 mm, which promotes the flow maldistribution as well.

4.2 The optimized experimental model

4.2.1 Zero cooling load simulation

The model is now used to predict a better operational condition. As explained, improvements are made by eliminating the dead time and reducing the τ_{mag} to 0.25 s. The obtained T_{span} at zero cooling load from the simulation is shown in Fig. 4.10 (for some different V^* at three different f ; 0.5 Hz, 1 Hz, and 1.25 Hz).

Shortening τ_{mag} and eliminating dead time, as illustrated in Fig. 3.5, makes the time required to transfer the same amount of heat in one cycle to become shorter. Parasitic heat loss to the environment in one cycle is also smaller with shorter cycle period. The system is indeed able to attain higher T_{span} of around 20 K at all frequencies, compared to 16 K for the original experimental setup. The T_{span} at 1 Hz is slightly higher than that of 0.5 and 1.25

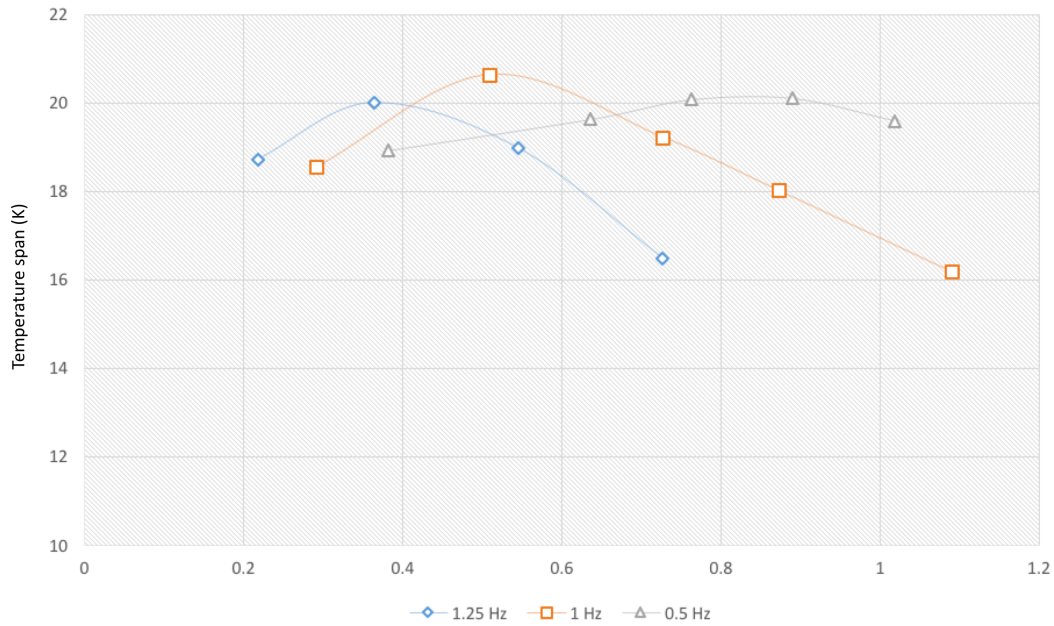


Figure 4.10: Temperature span versus the ratio of displaced fluid V^* at zero cooling load for various operating frequency

Hz.

There is an optimal point at which the T_{span} is the widest. For lower f , the optimum T_{span} at zero cooling load occurs at higher V^* . It may be related to the heat loss from the regenerator to the environment which makes that the working fluid needs to be displaced more to the reservoir. At higher f , the fluid flow period is very short which requires a high mass flow rate to sufficiently move the fluid to absorb or release the heat from or to the AMR.

The T-s diagram is again presented for the optimized Gd model to get the idea about the cycle steps, as shown in Fig. 4.11. Each area in the figure represents the process done by the corresponding particle at a particular position in the AMR. One can notice that the largest area coincides at around Curie point, 293 K. The figure also indicates each step in a cycle with a different color line. The red line describes the magnetization, blue line for the hot blow, green line for the demagnetization, and pink line for the cold blow.

4.2.2 Cooling capacity

The optimized model can enhance the cooling capacity of the AMRR. Fig. 4.12 summarizes the predicted cooling capacity of the optimized Gd AMR model with 15 °C cooling load temperature at 1 Hz operating frequency f . The result is much better the experiment (see Fig. 3.2). It is related to the higher operating frequency in the optimized model that leads to a higher mass flow rate for the same ratio of displaced fluid (V^*). This situation consequently increases the cooling capacity. The model itself will always overestimating the cooling capacity since it assumes an ideal heat exchanger. Please refer to Appendix A.2 for the comparison of cooling capacity calculated by the model with the experimental measurement (at f 0.3 Hz and V^* 0.42).

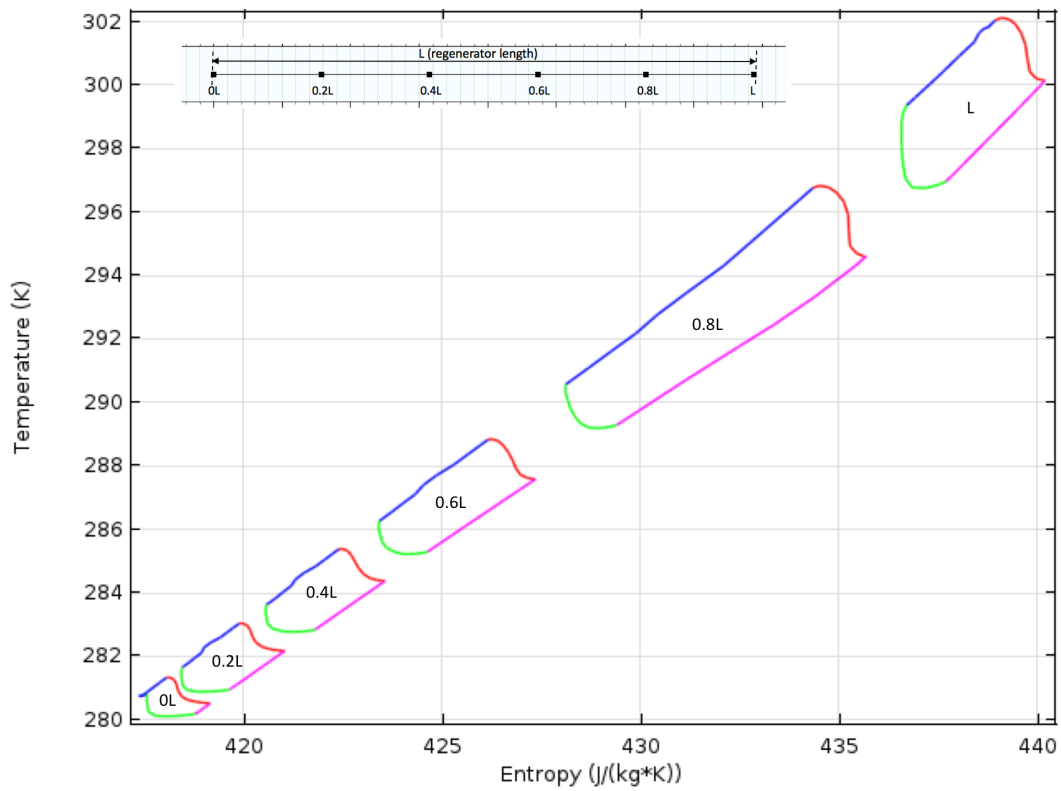


Figure 4.11: T-s diagram for a cycle at periodic steady state, improved Gd model f 1 Hz V^* 0.29

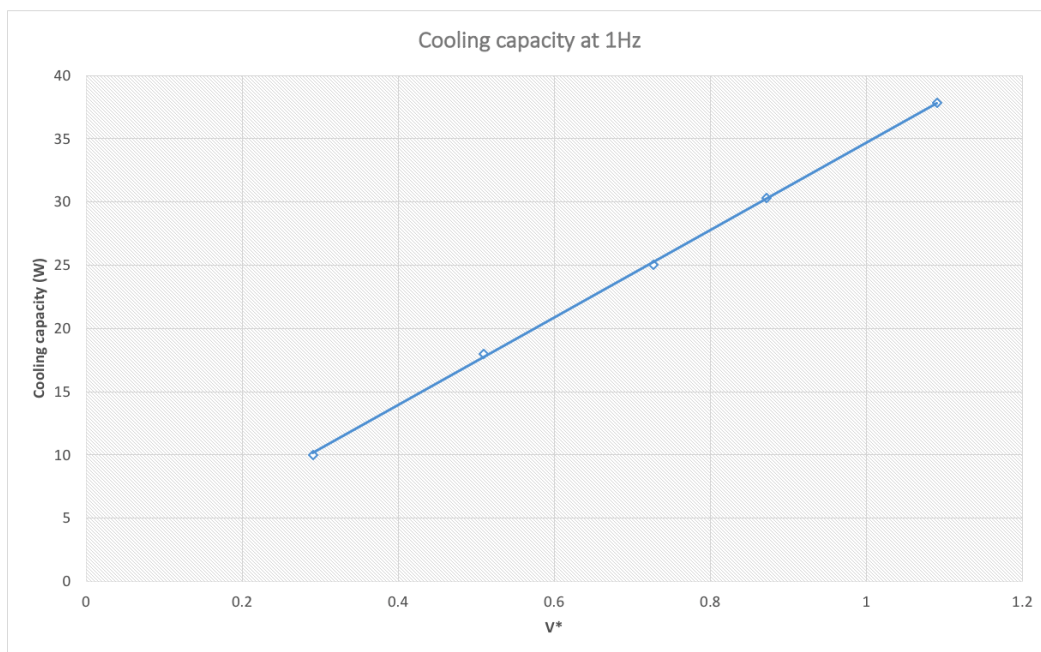


Figure 4.12: Cooling capacity at 15 deg C of cold temperature and f 1 Hz

4.3 Optimized model with layered $MnFe(P,Si)$ compound as MCM

In this set of simulations, the model is run with different MCM. The geometries are not altered; either in external dimension, porosity, or the spherical particle diameter; hence the hydrodynamic situation is similar. Since the MCM is changed from Gd to $Mn_{1.25}Fe_{0.7}(P_{1-y}Si_y)$ compound, there are differences in the magnetocaloric properties. The corresponding y values are 0.49, 0.50, 0.51, and 0.52.

Gadolinium, with its SOMT, keeps the temperature change in relatively considerable magnitude while operating at a wide range of initial temperatures, from 200 to 300 K. Contrary to Gd, $MnFe(P,Si)$ compound has First Order Magnetic Transition (FOMT) characteristic; hence a considerable ΔT_{ad} only appears at narrow temperature range, depending on the value of y .

4.3.1 The MCE in the layered AMR

As mentioned in Chapter 3, there might be an inaccuracy in simulating the magnetocaloric properties of the compound as the completion of the properties is done via a projection method and interpolation. The simulation suggests a different behavior of the adiabatic temperature change with the data provided by [21] as Curie point is shifted.

Table 4.1 summarizes Curie points defined by the data obtained from the projection which are included into the model of the layered AMR for $\mu_0 H$ from zero to 1.15T. Although deviating, it still has the variation of Curie temperature from 300 K to 277.5 K and still relevant to put them into the model to make a four-layered AMR. Fig. 4.13 shows the temperature change given by the model at different initial temperature with 0 to 1.15 Tesla of applied magnetic field.

Table 4.1: Curie point at different y value

| y value | 0.49 | 0.5 | 0.51 | 0.52 |
|-------------|---------|-------|-------|-------|
| T_{curie} | 277.5 K | 286 K | 296 K | 300 K |

It can be seen that for temperature 27 °C and $\mu_0 H$ 1.15 T, each section of the layer gives a different response, where the one with y 0.52 has the highest ΔT_{ad} . Another layer has its optimal ΔT_{ad} at another temperature. This situation is related to the heat generated by the MCE. The complete MCE heat source graphs is given in Appendix A.6.

Despite receiving heat four times higher, the compound temperature increase is not as high as Gd. The reason for this is that the heat capacity of the compound is also higher. According to Fig. 3.13, the approximate heat capacity of the compound can reach up to five times higher than Gd.

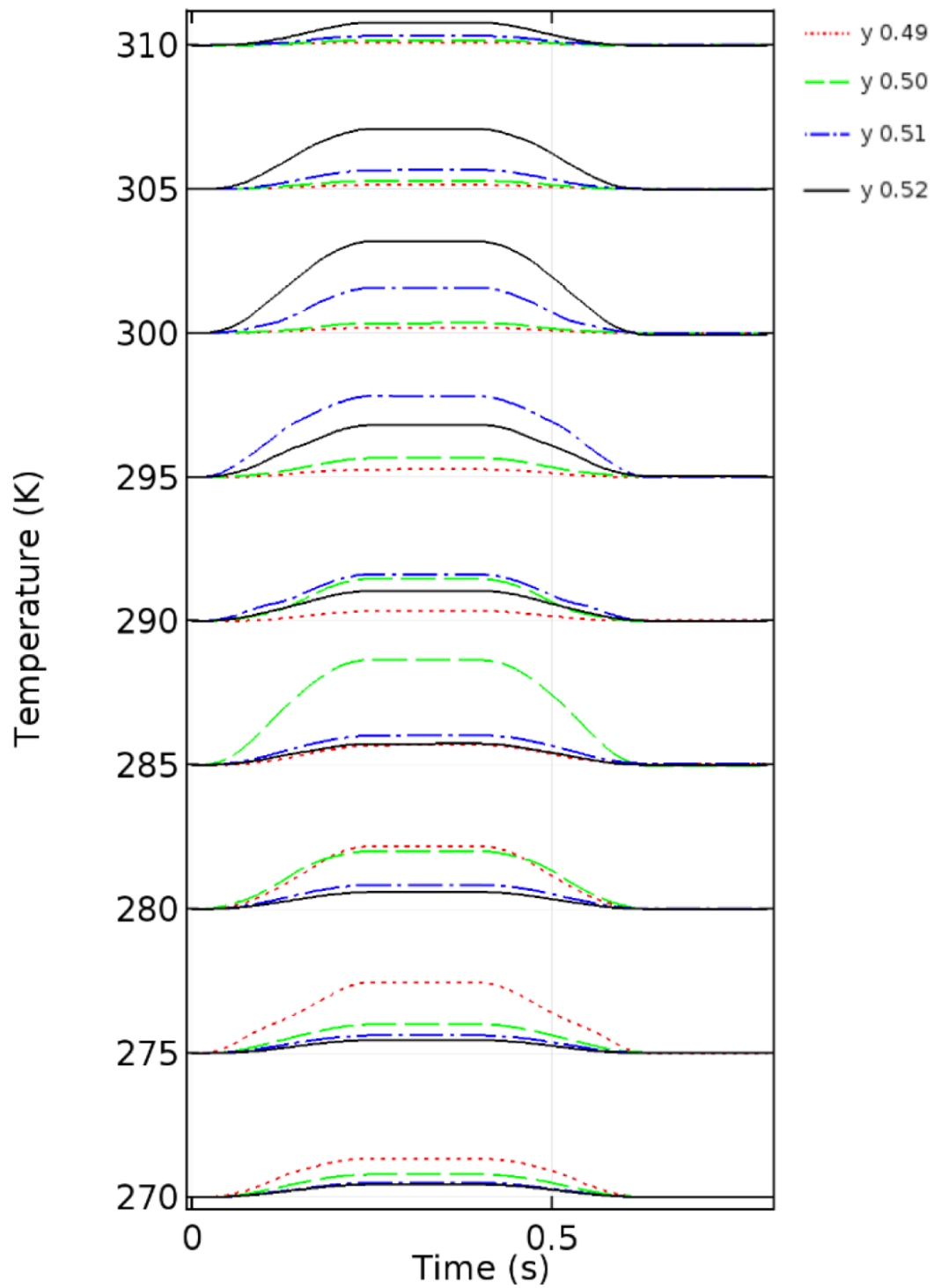


Figure 4.13: Temperature change for different y value and different initial temperature with $\mu_0 H$ zero to 1.15 T

4.3.2 Zero cooling load simulation

Temperature profile curve along the layered AMR in a cycle at periodic steady state is also not as smooth as for Gd, as depicted in Fig. 4.14. It occurs because of differences in the magnetocaloric characteristics between one layer and another. It is evident from the fact that the change of the curve trends (the ripple) occurs at the interface point between two layers, which are marked by the black dashed lines in the figure.

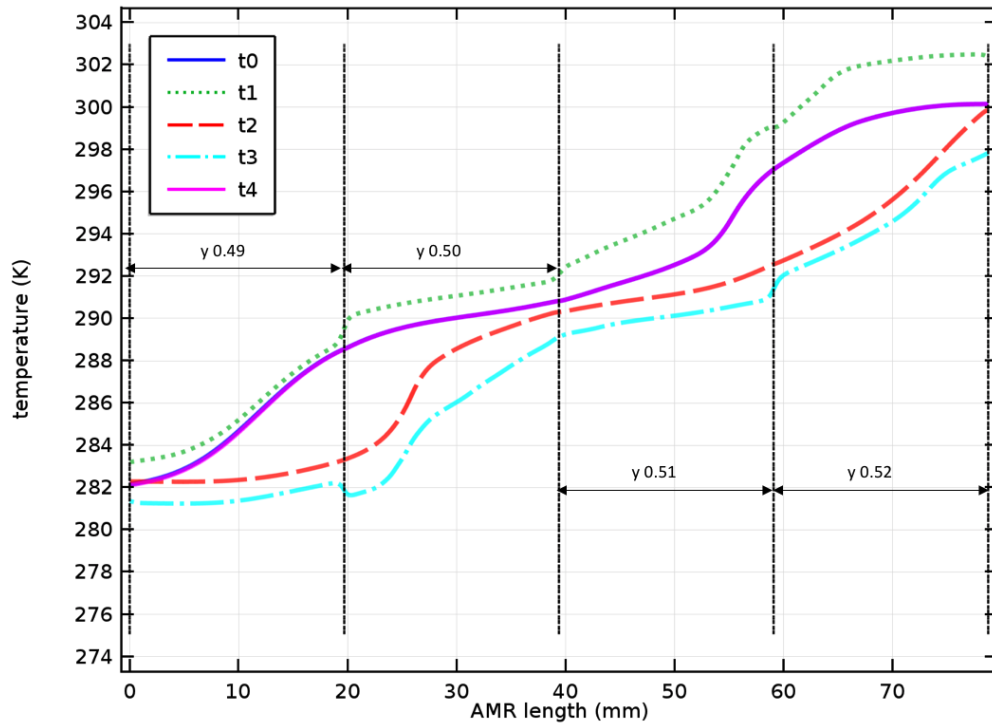


Figure 4.14: MCM temperature profile along AMR length at the end of every step in one cycle of periodic steady state at $f = 1$ Hz and $V^* = 0.44$ (t0-t1: magnetization, t1-t2: hot blow, t2-t3: demagnetization, t3-t4: cold blow)

It is also evident that the system failed to "activate" the coldest layer of the AMR. Even after the periodic steady state has been reached, the cold end does not operate at its best condition. It might be related to the length of the regenerator that is not optimal for the four layers configuration. It is also interesting to see how the system will respond if more layer with suitable T_{curie} are added to the regenerator.

The simulations (which gives the profile in Fig. 4.14) started with initial temperature of 300.15 K. The simulation has also been repeated with an initial temperature profile matching better to the Curie temperatures of the different MCM layers. However, it eventually gives the similar temperature profiles to those shown in Fig. 4.14, as indicated by Fig. 4.15. This shows that the results is independent of the initial temperature profile. It also shows that there is a mismatch of the four different materials.

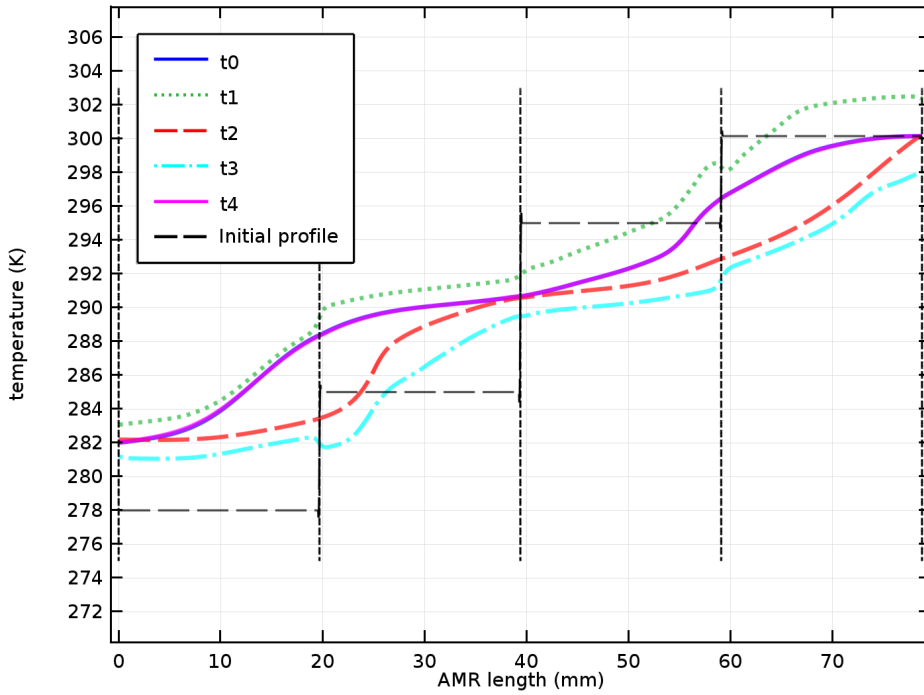


Figure 4.15: MCM temperature profile along AMR length with initial temperature at f 1 Hz and V^* 0.44 (t0-t1: magnetization, t1-t2: hot blow, t2-t3: demagnetization)

Temperature span at zero cooling load

Fig. 4.16 summarizes the T_{span} of the AMR with four layers of MnFe(P,Si) compound at three different f for various V^* . The span is apparently slightly lower than the one with Gd. It is also noticed that, by interpolation of the point, the optimum V^* that gives best T_{span} is similar for all three f , at around 0.47.

The layered $Mn_{1.25}Fe_{0.7}(P_{1-y}Si_y)$ compound is unable to match the temperature span of the Gd AMR because the maximum ΔT_{ad} of the compound at 1.15 T is lower than Gd. This is also because the layered AMR not operates at its best condition as a layer near the cold end gives low temperature change when it is (de)magnetized, as explained in the second paragraph of this subsection.

Time to reach periodic steady state

An interesting result from the simulation is the time needed to reach a periodic steady state. In general, the layered AMR model reaches periodic steady state much faster compared to the Gd AMR, as shown in Fig. 4.17. It might be related to the layered structure characteristics. The difference of magnetocaloric properties on each layer promotes the creation of temperature profile along the AMR length.

4.3.3 Cooling capacity

The cooling capacity presented in this subsection is calculated at the same f and cooling load temperature, i.e. 1 Hz and 15 °C, as in Subsection 4.2.2. Therefore the comparison

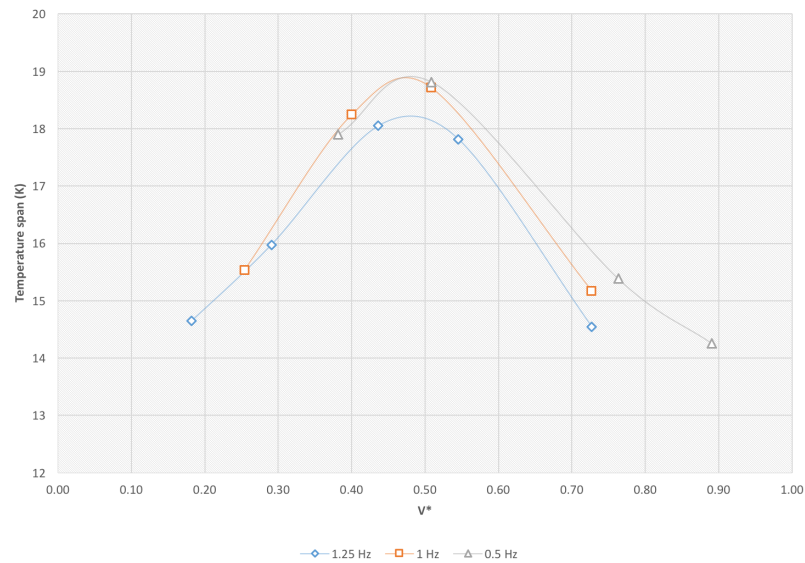


Figure 4.16: T_{span} at various V^* of AMR with MnFe(P,Si) compound for 0.5 Hz, 1 Hz, and 1.25 Hz of operating frequency.

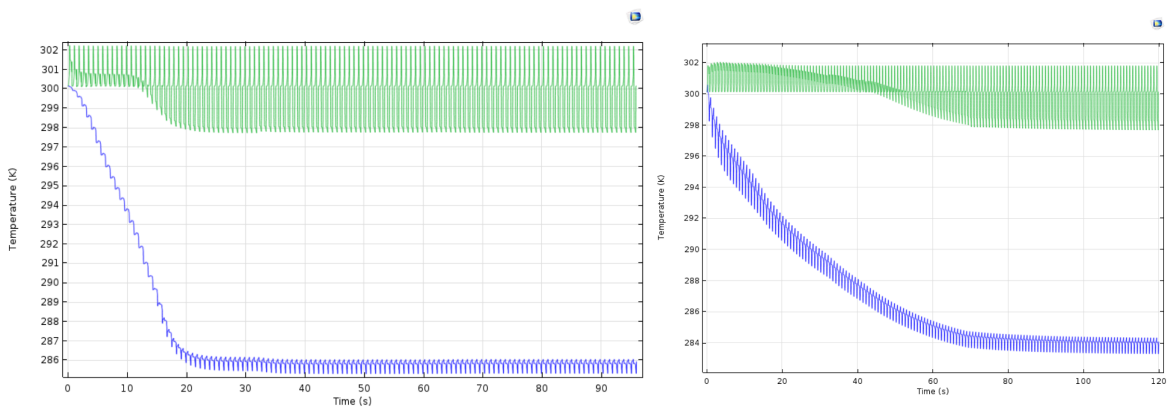


Figure 4.17: Temperature at hot end (green line) and cold end (blue line) for layered AMR (left) and optimized Gd AMR (right) at $f = 1.25$ Hz $V^* = 0.73$

between the two can be carried out. The simulation suggests that, for V^* larger than 0.3, the maximum cooling capacity in the layered AMR is better than the Gd AMR at the same operating condition, as depicted in Fig. 4.18.

Refer to Fig. 4.19, the layered AMR has wider temperature swing at the cold end than the Gd AMR at similar operating condition. In other words, the temperature of the fluid that goes into the CHEX in layered AMR is lower than that in Gd AMR, while the CHEX outlet temperature is the same, 15 °C. This is because a layer in the layered AMR has higher adiabatic temperature change due to the magnetocaloric effect at the assigned cooling load temperature (15 °C). Also, the heat capacity of the compound is much higher than Gadolinium, which makes the temperature of the working fluid decreasing to a lower temperature than that in Gd AMR during the cold blow.

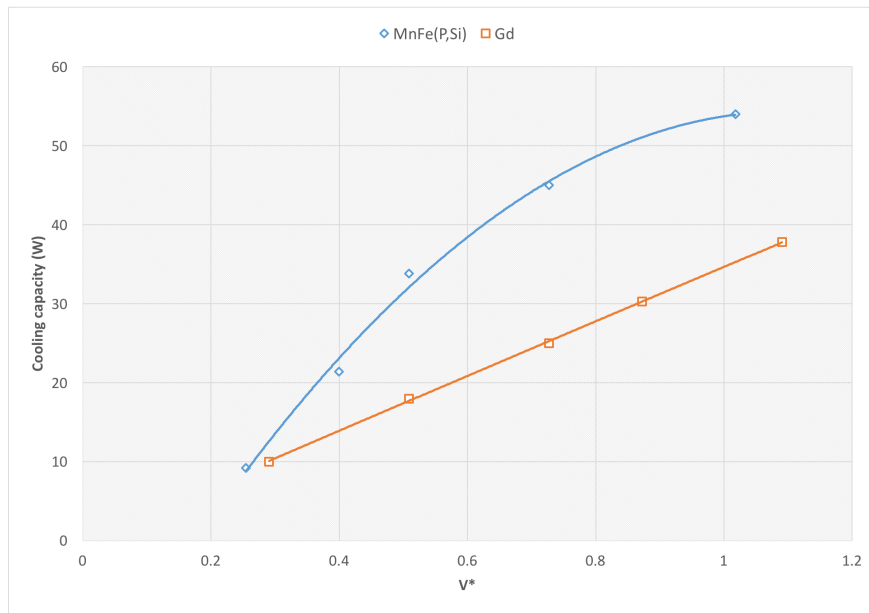


Figure 4.18: Comparison of cooling capacity of Gd AMR and layered MnFe(P,Si) compound AMR

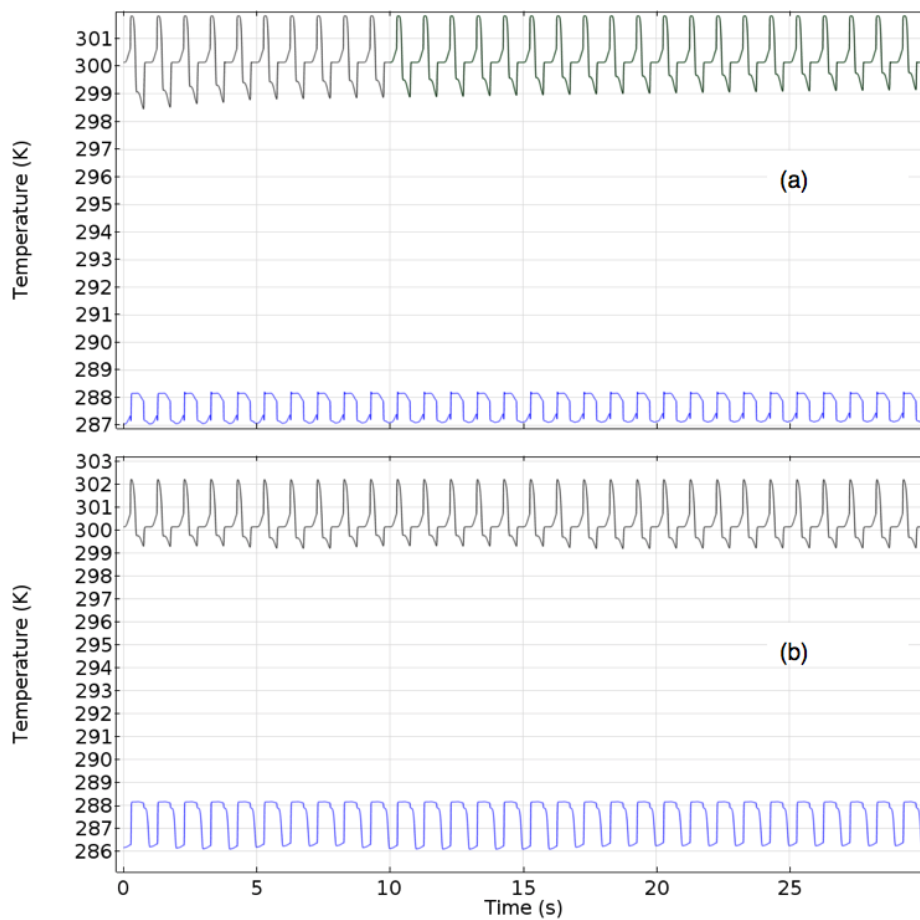


Figure 4.19: The fluid temperature fluctuation at hot end (black line) and cold end (blue line) in Gd AMR (a) and the layered AMR (b)

Conclusions and recommendations

5.1 Conclusions

In this work, a model built by COMCOL Multiphysics software is used to investigate and predict the performance of active magnetic regenerative refrigeration (AMRR) system with packed-bed regenerator. Uniform spherical particles form the packed-bed. The particles made from two different magnetocaloric material, Gadolinium (Gd) and four layers of MnFe(P,Si) compound. Firstly, the model with Gd is verified by comparing its results with a reference experimental result. Secondly, the performance of the Gadolinium packed-bed AMRR is compared to the one with layered MnFe(P,Si) compound. The referred performance parameter in this study is the maximum temperature span and the cooling capacity.

Concerning the first research question, the one-dimensional model of the magnetocaloric heat pump or refrigeration system with packed-bed regenerator is representative. The model simulation results show good agreement with the experimental reference. The model not only predicts correct trends, but also it predicts the absolute value of temperature span accurately.

The rough magnetocaloric properties input data with various interpolations is not good enough for calculation accuracy and consistency. The model failed to maintain the energy balance as the heat that goes into the MCM (due to MCE) is not fully described by the changes of internal energy. The balance can be maintained if the model uses data of heat capacity of Gadolinium that are independent to the applied magnetic field. However, that is not true for a magnetocaloric effect case. This unexpected consequences also have been noticed in the previous thesis work of [5] and [26] which uses the same method.

As to the second research question regarding the comparison of the performance of packed-bed AMR with MnFe(P,Si) compound to the Gd AMR, the model predicts that the system with layered compound has slightly lower temperature span at zero cooling load. However, the layered AMR is superior to the Gd AMR on the cooling capacity when a cooling load is applied to the system. At cooling load temperature of 15 °C, the layered AMR has a greater cooling capacity than Gd AMR because at 15 °C cooling load temperature, the MnFe(P,Si) compound has a wider temperature change due to MCE than Gadolinium.

This study also shows the giant magnetocaloric effect from a material with the first order

magnetic phase transition (the MnFe(P,Si) compound). The heat generated by the MCE is up to five times larger than that of the second order material (Gd). However, the result still needs to be verified, especially related to the magnetocaloric properties of the MnFe(P,Si) compound. This study made a very broad and general prediction of magnetocaloric properties of the compound by assumption and interpolation which likely leads to inaccuracies. It creates some differences of its magnetocaloric property to the reference MnFe(P,Si) compound.

5.2 Recommendations

Improvements can be made to this thesis work for future study. Resolving the thermodynamic inconsistencies is an important thing that must be addressed. One of the methods is by applying the Mean Field Theory to predict the magnetocaloric properties of the material. The another way is by using a smooth measurement magnetocaloric properties data, if available.

A one-dimensional model neglects the variation of velocity in the direction perpendicular to the fluid mainstream direction. It might not always reflect reality since a real packed-bed regenerator will always have particles uniformities which cause a flow maldistribution. Further, it also affects the heat transfer. To form the MCM into a uniform spherical geometry is not a simple task since it depends on its formability. The model can be upgraded to a two-dimensional model or by assuming a particular correction factor in Nusselt number prediction.

As explained by [9], another important issue is the demagnetization field. It makes the internal magnetic field in the MCM body to be lower than the applied magnetic field. A correction factor to the applied magnetic field might need to be considered for a more accurate prediction.

Improvement is also necessary for the magnetocaloric properties data collection of the MnFe(P,Si) compound. During the process of this thesis, the publications that provide complete data on the magnetocaloric properties of the compound was not sufficiently gathered. Cooperation is necessary with relevant parties to obtain a good, complete, and accurate magnetocaloric properties. The data extraction from graph to numbers has to be done with a better precision .

The study can also be extended to the variation of regenerator geometries, either in the length or the particle diameter or porosity. It is also interesting to see the performance of layered AMR with different layer configuration. Variation can be made by making more than four layers in the AMR.

Bibliography

- [1] “Web site of the European Commission.” [Online]. Available: <https://ec.europa.eu/energy/en/topics/energy-efficiency/heating-and-cooling>
- [2] J. Bollen, C. Brink, H. Eerens, A. Manders *et al.*, “Co-benefits of climate policy.” *Co-benefits of climate policy*, 2009.
- [3] M. Isaac and D. P. Van Vuuren, “Modeling global residential sector energy demand for heating and air conditioning in the context of climate change,” *Energy policy*, vol. 37, no. 2, pp. 507–521, 2009.
- [4] R. Teverson, T. Peters, M. Freer, J. Radcliffe, L. Koh, T. Benton, D. McLeod, S. Uren, R. Elliot, P. Fryer *et al.*, “Doing cold smarter,” 2015.
- [5] J. Stoter, “Modeling of a magnetocaloric heat pump in comsol,” 2016.
- [6] W. Goetzler, R. Zogg, J. Young, and C. Johnson, “Energy savings potential and rd&d opportunities for non-vapor-compression hvac technologies,” *Navigant Consulting Inc., prepared for US Department of Energy*, 2014.
- [7] A. Smith, “Who discovered the magnetocaloric effect?” *The European Physical Journal H*, vol. 38, no. 4, pp. 507–517, 2013.
- [8] J. R. Gómez, R. F. Garcia, A. D. M. Catoira, and M. R. Gómez, “Magnetocaloric effect: A review of the thermodynamic cycles in magnetic refrigeration,” *Renewable and Sustainable Energy Reviews*, vol. 17, pp. 74–82, 2013.
- [9] A. Kitanovski, J. Tušek, U. Tomc, U. Plaznik, M. Ozbolt, and A. Poredoš, *Magnetocaloric Energy Conversion*. Springer, 2015, vol. 565.
- [10] K. K. Nielsen, “Numerical modeling and analysis of the active magnetic regenerator,” 2010.
- [11] A. Kitanovski and P. W. Egolf, “Thermodynamics of magnetic refrigeration,” *International Journal of Refrigeration*, vol. 29, no. 1, pp. 3–21, 2006.
- [12] J. Tušek, A. Kitanovski, S. Zupan, I. Prebil, and A. Poredoš, “A comprehensive experimental analysis of gadolinium active magnetic regenerators,” *Applied Thermal Engineering*, vol. 53, no. 1, pp. 57–66, 2013.

- [13] D. A. Nield and A. Bejan, *Convection in porous media*. Springer Science & Business Media, 2006.
- [14] M. Kaviany, *Principles of Heat Transfer in Porous Media*. Springer, 1995.
- [15] N. Wakao and S. Kagei, *Heat and mass transfer in packed beds*. Taylor & Francis, 1982, vol. 1.
- [16] U. Plaznik, J. Tušek, A. Kitanovski, and A. Poredoš, "Numerical and experimental analyses of different magnetic thermodynamic cycles with an active magnetic regenerator," *Applied Thermal Engineering*, vol. 59, no. 1, pp. 52–59, 2013.
- [17] J. Tušek, A. Kitanovski, I. Prebil, and A. Poredoš, "Dynamic operation of an active magnetic regenerator (amr): numerical optimization of a packed-bed amr," *International Journal of Refrigeration*, vol. 34, no. 6, pp. 1507–1517, 2011.
- [18] M. Ivan, "Assessment of magnetic cooling for domestic applications," 2012.
- [19] K. Engelbrecht, G. Nellis, and S. Klein, "A numerical model of an active magnetic regenerator refrigeration system," in *Cryocoolers 13*. Springer, 2005, pp. 471–480.
- [20] S. Y. DanKov, A. Tishin, V. Pecharsky, K. Gschneidner *et al.*, "Magnetic phase transitions and the magnetothermal properties of gadolinium," *Physical Review B*, vol. 57, no. 6, p. 3478, 1998.
- [21] H. Yibole, F. Guillou, L. Zhang, N. H. van Dijk, and E. Brück, "Direct measurement of the magnetocaloric effect in Mn Fe(P, X)(X=As, Ge, Si) materials," *Journal of Physics D: Applied Physics*, vol. 47, no. 7, p. 075002, 2014.
- [22] Dynalene, "Dynalene ethylene glycol series," 2014.
- [23] N. Thang, X. Miao, N. van Dijk, and E. Brück, "Structural and magnetocaloric properties of (Mn, Fe)₂ (P, Si) materials with added nitrogen," *Journal of Alloys and Compounds*, vol. 670, pp. 123–127, 2016.
- [24] H. D. Nguyen, *Moment formation and giant magnetocaloric effects in hexagonal Mn-Fe-P-Si compounds*. TU Delft, Delft University of Technology, 2012.
- [25] K. Engelbrecht, J. Tušek, K. K. Nielsen, A. Kitanovski, C. R. Bahl, and A. Poredoš, "Improved modelling of a parallel plate active magnetic regenerator," *Journal of Physics D: Applied Physics*, vol. 46, no. 25, p. 255002, 2013.
- [26] W. de Vries, "Application of peltier thermal diode in a magnetocaloric heat pump," 2016.
- [27] G. Porcari, K. Morrison, F. Cugini, J. Turcaud, F. Guillou, A. Berenov, N. Van Dijk, E. Brück, L. Cohen, and M. Solzi, "Influence of thermal conductivity on the dynamic response of magnetocaloric materials," *International Journal of Refrigeration*, vol. 59, pp. 29–36, 2015.

- [28] L. von Moos, C. Bahl, K. K. Nielsen, and K. Engelbrecht, "Hysteresis in magnetocaloric materials: An experimental and modelling approach," Ph.D. dissertation, Technical University of Denmark Danmarks Tekniske Universitet, Risø National Laboratory for Sustainable Energy Risø Nationallaboratoriet for Bæredygtig Energi, 2014.
- [29] T. Lei, K. Engelbrecht, K. K. Nielsen, and C. T. Veje, "Study of geometries of active magnetic regenerators for room temperature magnetocaloric refrigeration," *Applied Thermal Engineering*, 2015.

Appendix

A.1 General heat transfer correlation

The summary of some heat transfer quantitative correlation is presented in this appendix section. Those correlations are the Reynolds number, Prandtl number, Nusselt number, and the interstitial heat transfer coefficient. Fig. A.2 and A.3 shows all those correlation, respectively. All those correlations are evaluated at a periodic steady state condition for Gd improved model with f 1 Hz and V^* 0.73. Fig. A.1 (left) shows the corresponding temperature profile along the AMR length (including the position identification). It is also evident that for fluid velocity higher than 50 mm/s, the lumped capacitance condition is not applied to the AMR spherical particles since the value of Bi has exceeds 0.1.

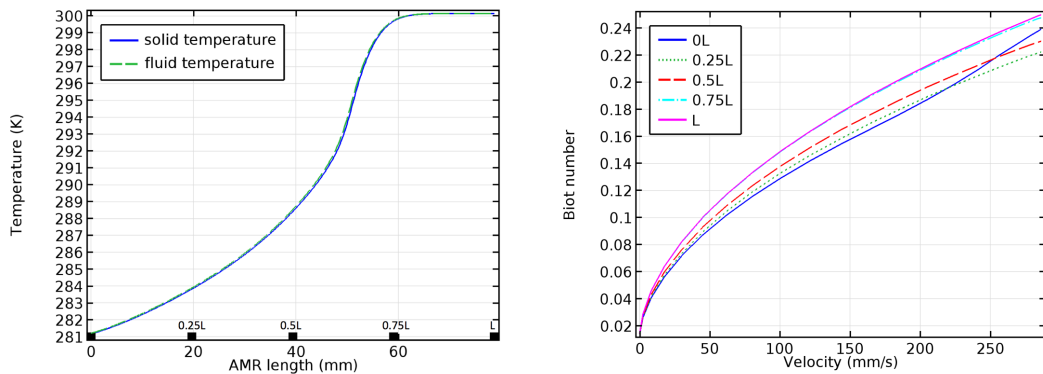


Figure A.1: Temperature profile (left) and Biot number (right)

Compared to the calculated Nu presented by [29], as can be seen in Fig. A.4, the predicted value of Nu in this study is relatively high. The geometrical characteristic of regenerator in [29] is slightly different with d_h 0.2 mm and ε 0.36. The d_h of the model in this thesis is 0.18 mm with ε 0.349.

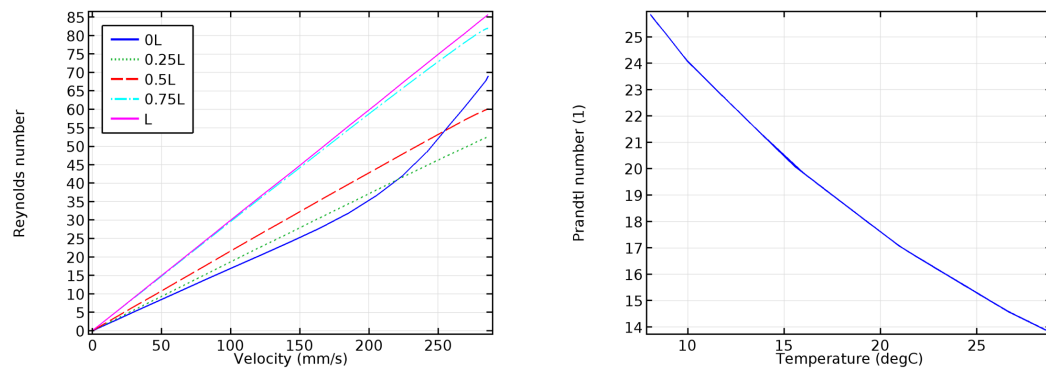


Figure A.2: Reynolds number as a function of the fluid velocity (left) and Prandtl number as a function of the fluid temperature (right)

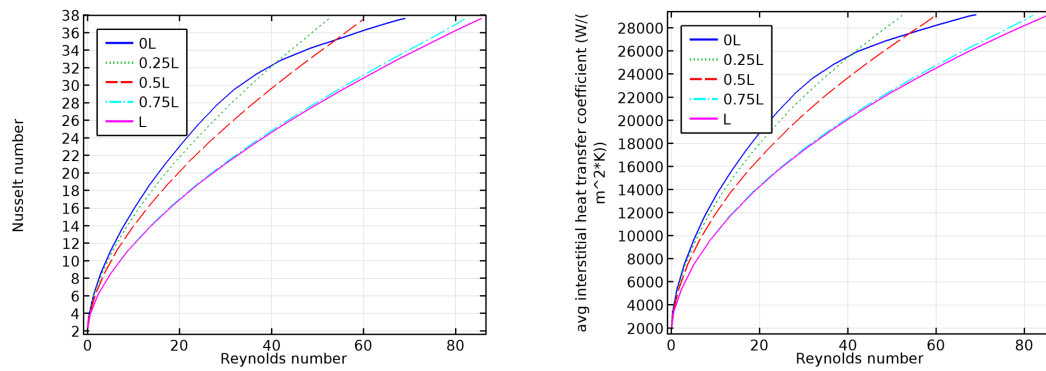


Figure A.3: Nusselt number as a function of Reynolds number (left) and heat transfer coefficient as a function of Reynolds number (right)

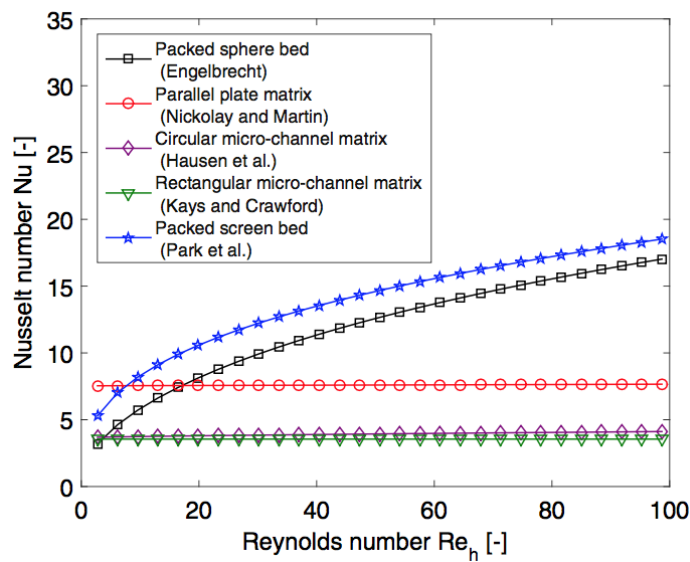


Figure A.4: Nusselt number of different AMR geometries with ε 0.36 and hydraulic diameter d_h 0.20 mm [29]

A.2 Cooling capacity at f 0.3 Hz

The experimental report of [12] gives the results for cooling capacity measurement and calculation of predicted COP. The magnetic work was not measured in the experiment; it was calculated instead. The calculation result, together with the measured cooling capacity, plug into Eq. 2.33 to estimate the COP of the system. Based on data extracted from Fig. 3.2, the sum of the calculated input work is around 0.48 W.

The available result for cooling capacity \dot{Q}_C and COP is only for 0.3 Hz. One may think that there just a slight difference between 0.3 Hz and 0.33 Hz. In fact, the fluid flow period is significantly different, i.e. 0.25 s at 0.33 Hz and 0.5 s at 0.3 Hz. The corresponding mass flow rate and applied magnetic field profile for f 1 Hz are depicted in Fig. A.5.

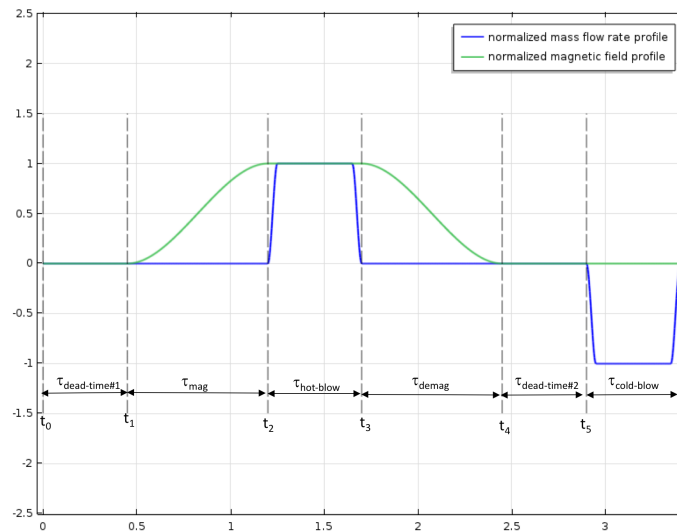


Figure A.5: Normalized profile of applied magnetic field and mass flow rate for f 0.3 Hz

The model developed in this study is also use to run a simulation at f 0.3 Hz and V^* 0.42 and predict the \dot{Q}_C . Firstly, the model runs in a zero cooling load condition to find out the maximum temperature span. The predicted temperature span (15 K) is higher than the experimental result (14 K). The cooling capacity obtained from the model is presented in Fig. A.6. The calculated pumping power, \dot{W}_{pump} is around 0.1 W (with \dot{m}_f 0.009 kg/s).

It shows in Fig. A.6 that the model is overestimating the cooling capacity. It might be related to the assumption of an ideal heat exchanger in the model. The outlet fluid temperature (from CHEX) is deemed to be equal to the cooling load temperature. In the experimental setup, there might also be another heat losses in the pump piston, which the model did not account.

A.3 COP prediction

Fig. A.7 presents the predicted COP obtained from the optimized model with Gd AMR as well as the layered AMR. The trends by quadratic regression for both of the cases looks

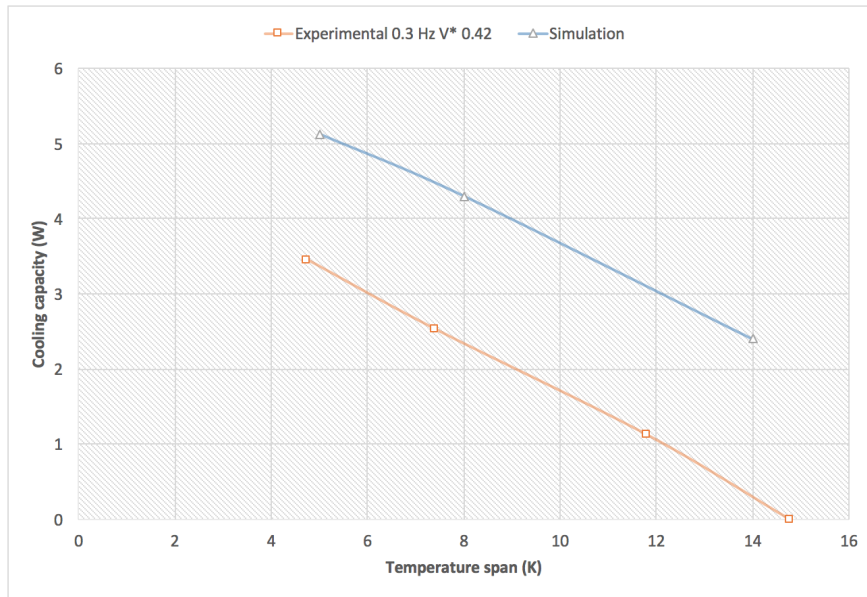


Figure A.6: Cooling capacity Vs. temperature span for experimental measurement and numerical model simulation

similar. The curve passes the peak when the V^* is higher than 0.8, which incorporated to mass flow rate of 0.04 kg/s. At that point, the corresponding pumping work is more than 2.3 W (see Section A.4).

There are several methods to predict the magnetic power input (\dot{W}_{mag}). In this thesis, the \dot{W}_{mag} is calculated based on Eq. 2.2. The report of [19] gives some suggestion on the method to calculate the \dot{W}_{mag} .

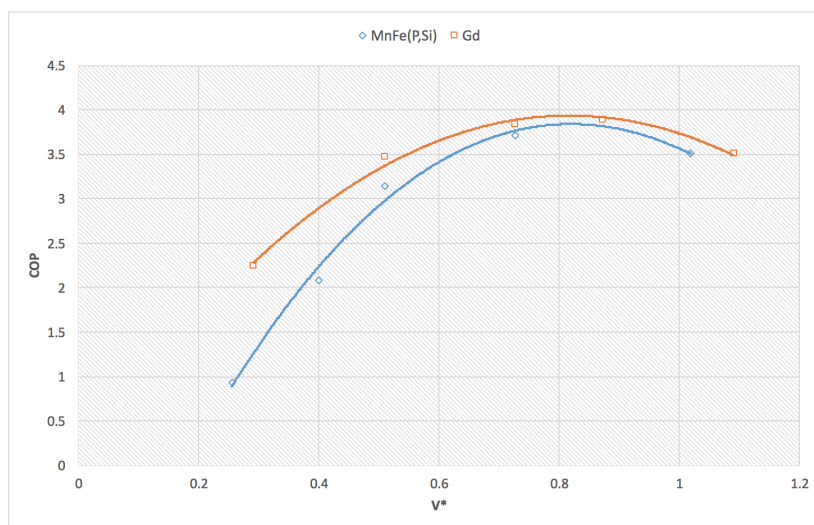


Figure A.7: Predicted COP of the Gd AMR and the layered AMR

A.4 Pumping work

In this section, the general relation between pumping work \dot{W}_{pump} with the mass flow rate is presented. Since the pump motor efficiency is assumed to be constant at 0.8, the another variable that determines the pumping is the fluid density. The variation of fluid density at the corresponding working temperature considerably small (see Fig. A.8), therefore it is relevant to compare the pumping work to the mass flow rate directly.

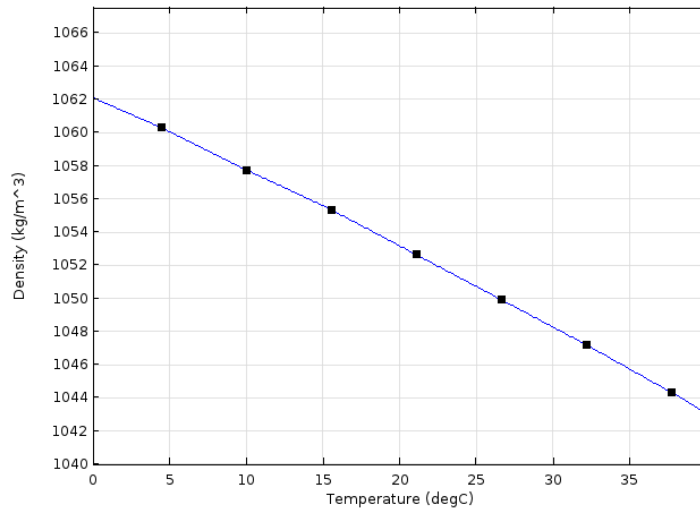


Figure A.8: Fluid density Vs. Temperature

Fig. A.9 depicts the development of pressure drop. Fig. A.10 reveal that the pumping work seems to increase by square growth as the mass flow rate increase. It can be understood as the value of \dot{W}_{pump} is parallel to the pressure drop, and pressure drop is parallel to the square of velocity.

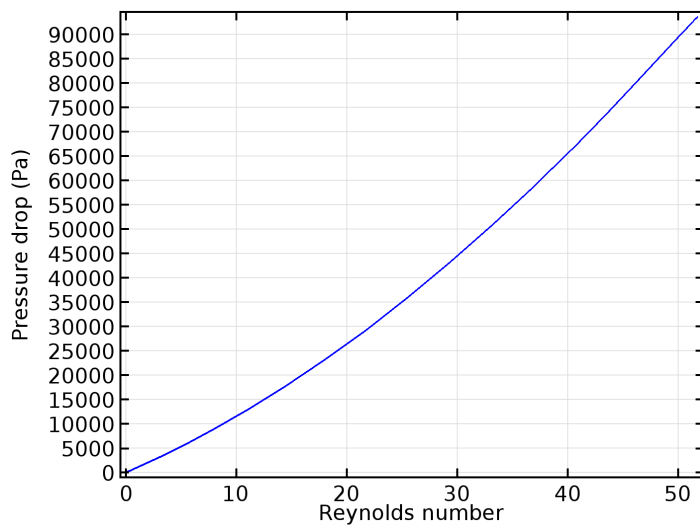


Figure A.9: Pressure drop as a function of Re

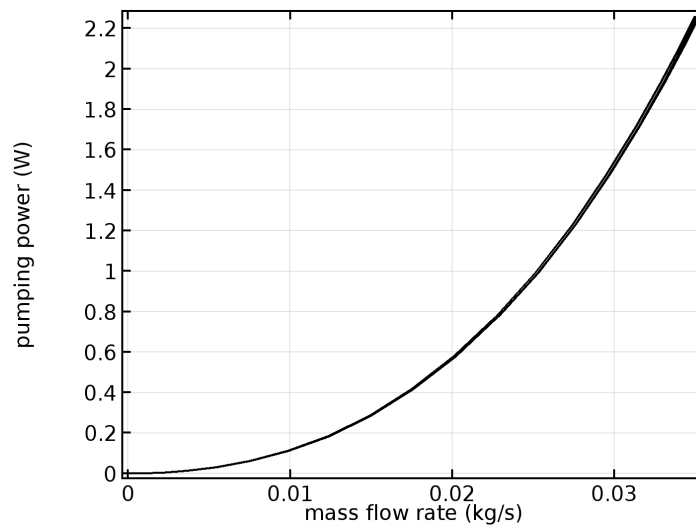


Figure A.10: Mass flow rate vs pumping work

A.5 Parasitic heat loss

Parasitic heat loss to the environment included to the models using thermal resistance, following the information from [25]. Fig. A.11 depict the heat loss at five different points along AMR length in a cycle at periodic steady state with f 1 Hz and V^* 0.73 (see Fig. A.1 (left)).

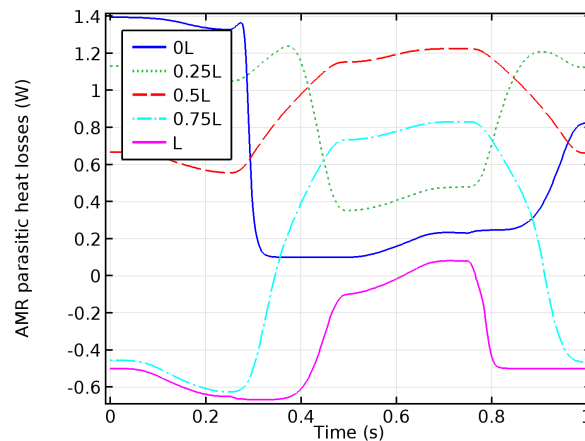


Figure A.11: Parasitic heat transfer to (or from) the environment

A.6 Magnetocaloric properties of the material in the model

The MCE included to the model via heat source which depends on the data of magnetization as a function of temperature and applied magnetic field. The heat capacity is also needed to solve the governing equation. This chapter gives additional information on the properties of the Gd and MnFe(P,Si) compound that put into the model, including the data obtained from interpolation and projection.

A.6.1 Gadolinium

The data availability of Gd properties is more than the compound. The data extraction is also better which creates a smooth curve of the volumetric heat source (\dot{Q}_{MCE}) as shown by Fig. A.12. The figure gives information on the range of temperature operation in which the MCE heat source is large enough. Based on the experimental measurement, Gadolinium has T_{curie} of 293 K, however, in the model the highest MCE heat source coincide at 296 K.

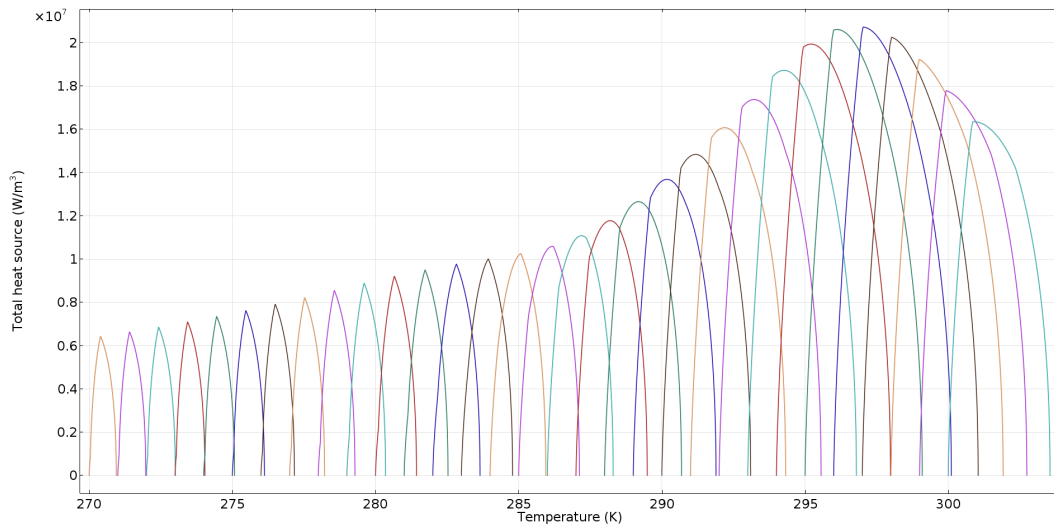


Figure A.12: MCE heat source of Gadolinium at different initial temperature for $\mu_0 H_0 = 1.15 \text{ Tesla}$

A.6.2 The compound

The projection and interpolation are taken to complete all required input data to get the model works with the layered AMR. The method is explained in detail in Chapter 3. Fig. A.13, A.14, and A.15 shows the approximate data for magnetization, while Fig. A.16 picture the estimation of the heat capacity for each y values at various applied magnetic field.

The result of MCE heat source that given by the model based on data projection and interpolation is presented in this subchapter, as shown in Fig. A.17, A.18, A.19, and A.20. The curve is wavy, not smooth as in Gd (Fig. A.12), which might be related to the ripple on the magnetization curve.

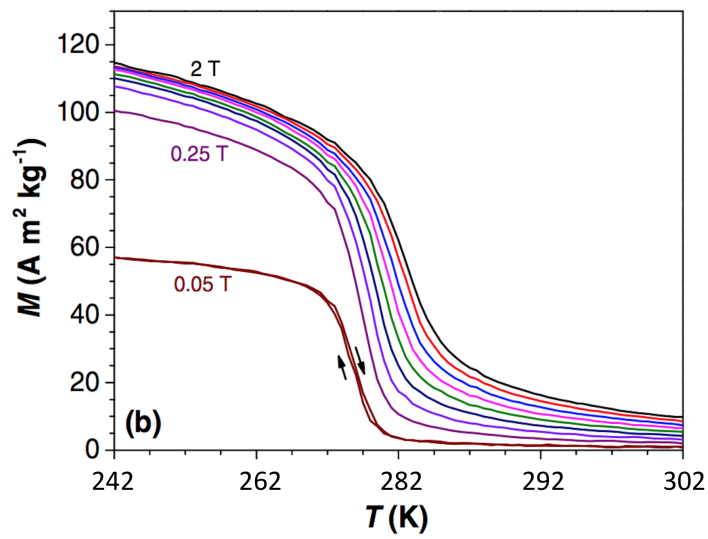


Figure A.13: Magnetization as a function of temperature at various applied magnetic field for y 0.49

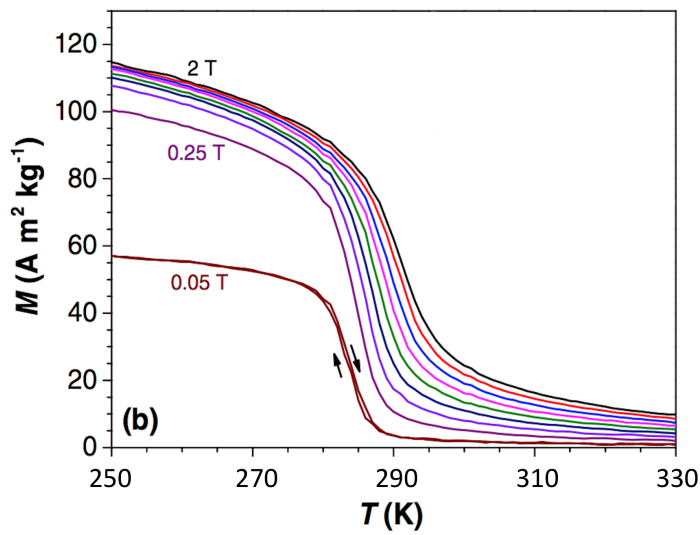


Figure A.14: Magnetization as a function of temperature at various applied magnetic field for y 0.50

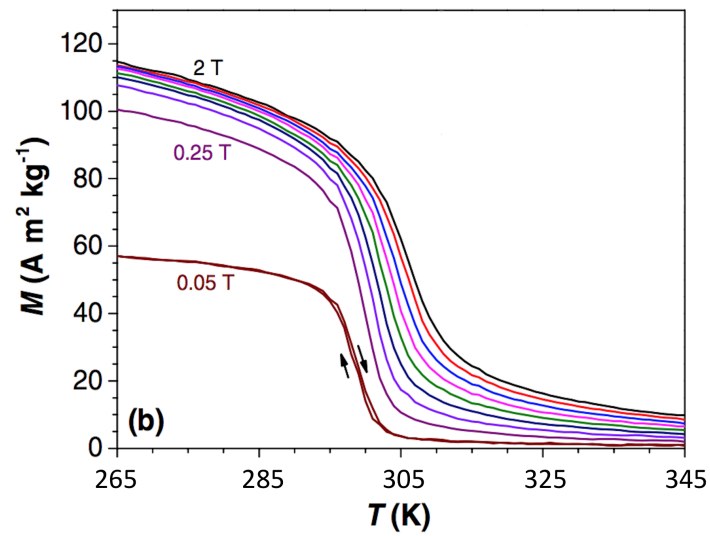


Figure A.15: Magnetization as a function of temperature at various applied magnetic field for $y = 0.52$

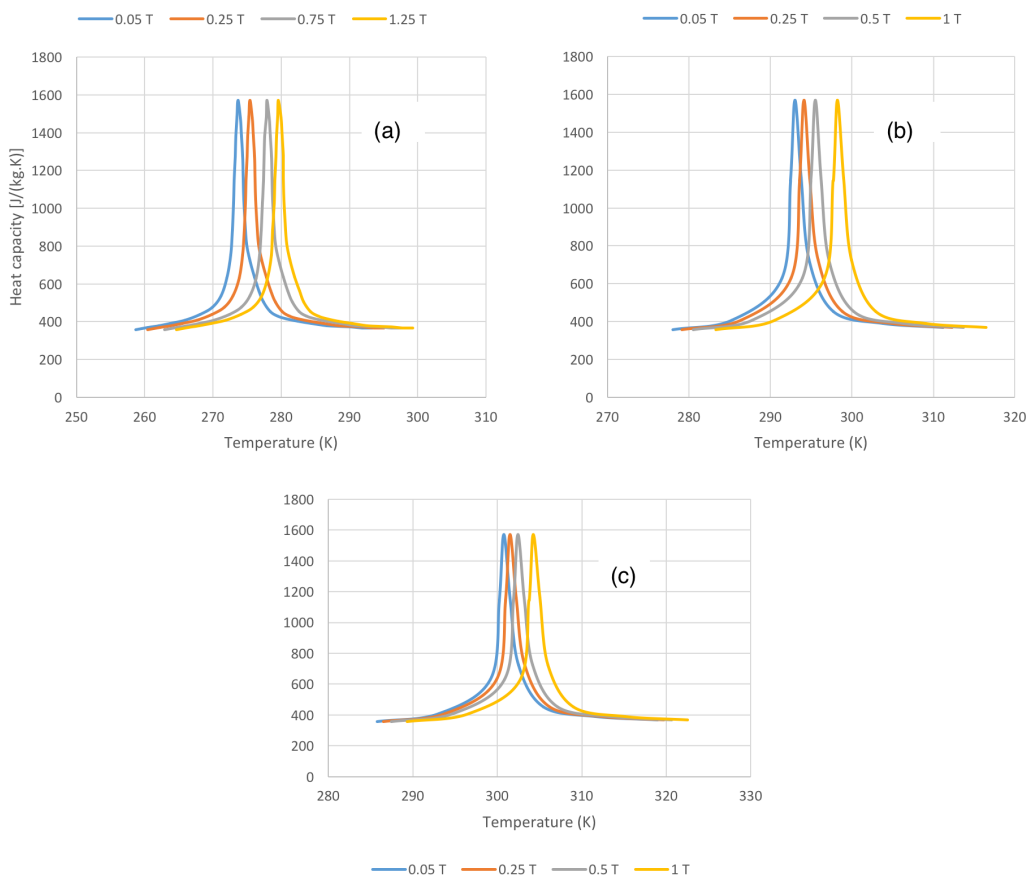


Figure A.16: Heat capacity as a function of temperature at various applied magnetic field for $y = 0.49$ (a), 0.51 (b), and 0.52 (c)

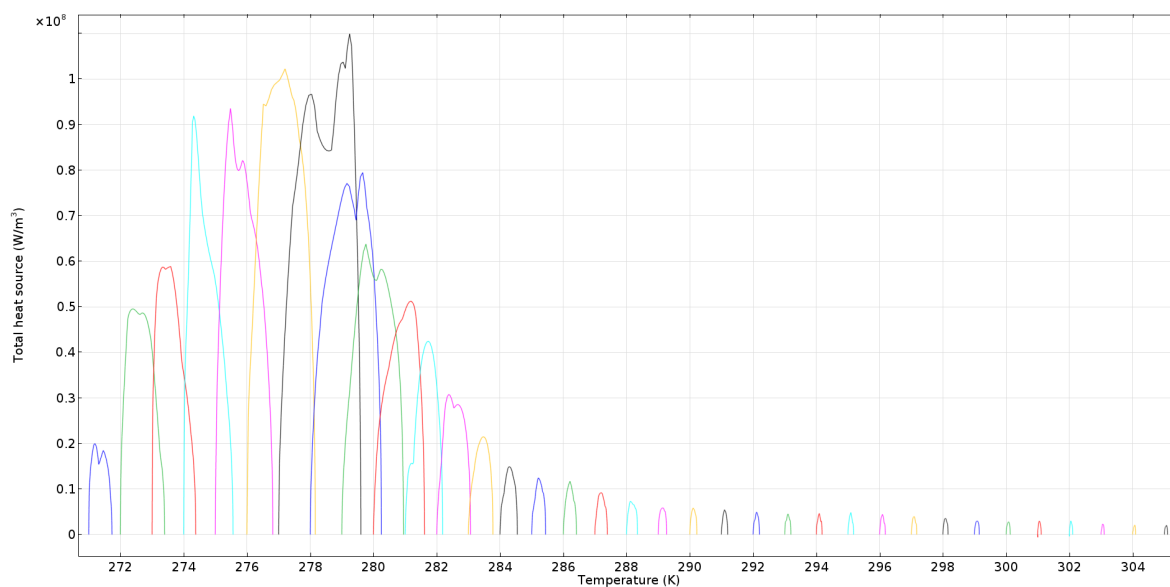


Figure A.17: MCE heat source of the compound with y values 0.49 in the model for $\mu_0 H_0 - 1.15 \text{ Tesla}$

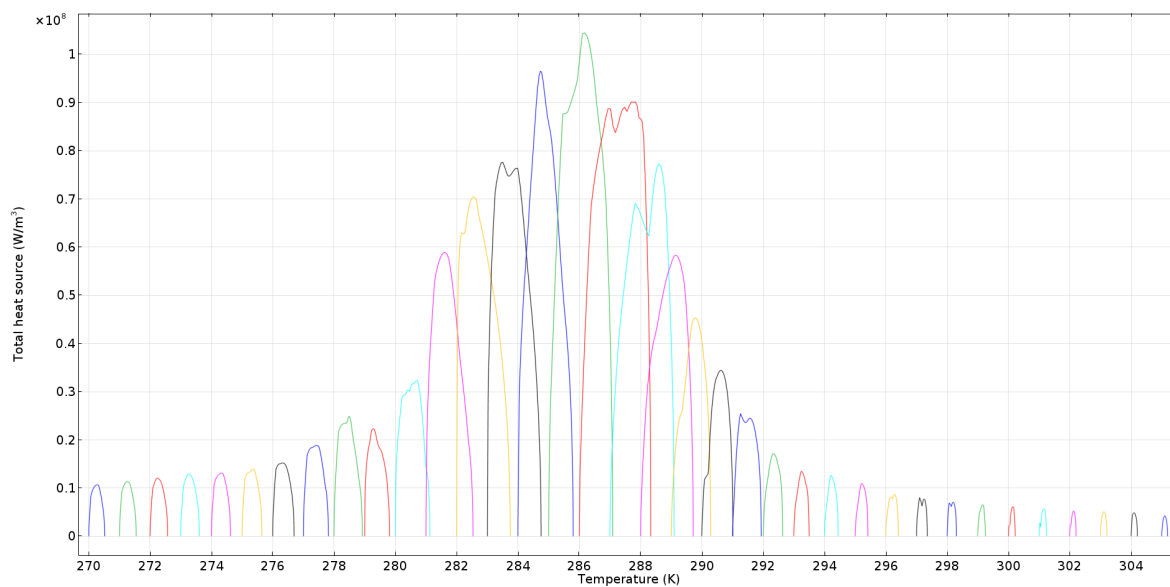


Figure A.18: MCE heat source of the compound with y values 0.50 in the model for $\mu_0 H_0 - 1.15 \text{ Tesla}$

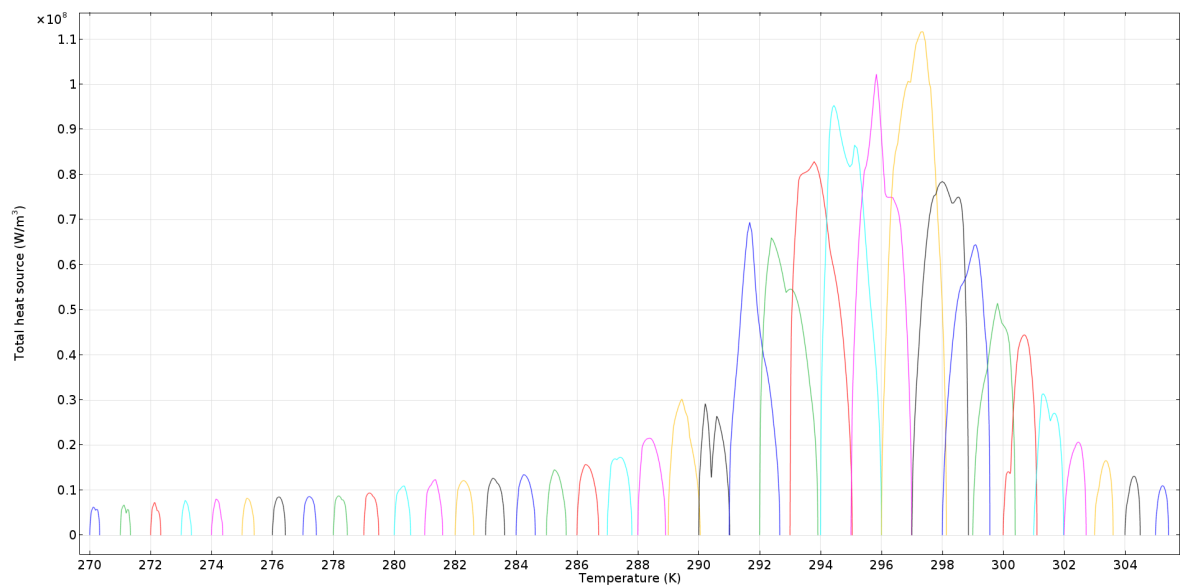


Figure A.19: MCE heat source of the compound with y values 0.51 in the model for $\mu_0 H_0 - 1.15 \text{ Tesla}$

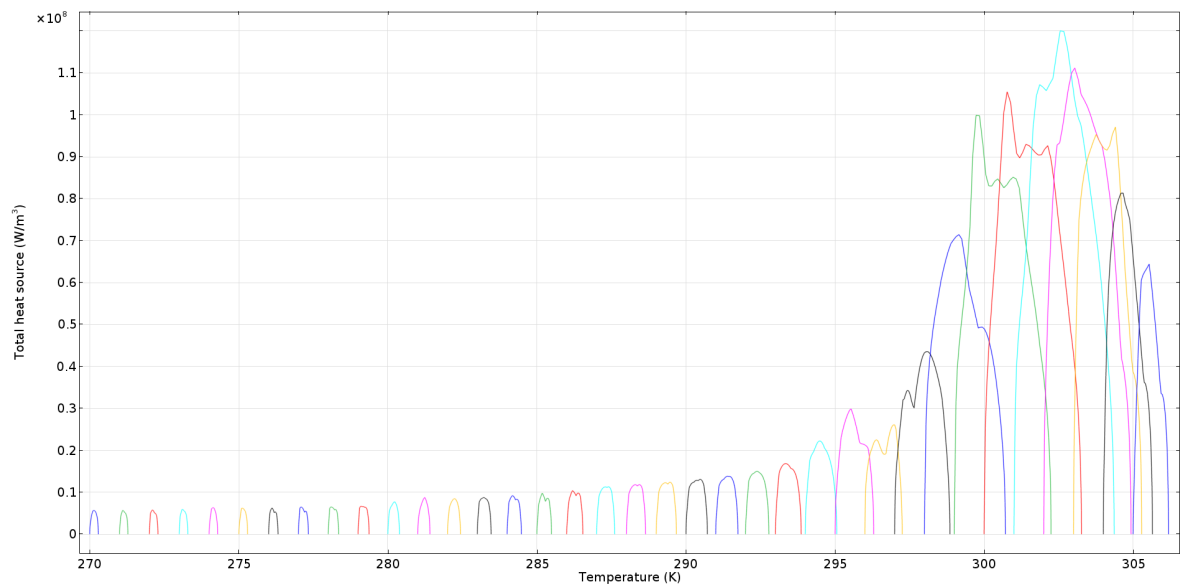


Figure A.20: MCE heat source of the compound with y values 0.52 in the model for $\mu_0 H_0 - 1.15 \text{ Tesla}$